Parameterizing the breaking and scattering of a mode-1 internal tide on abrupt step topography

by

Emma Christina Murowinski
B.Sc., Acadia University, 2010

A Thesis Submitted in Partial Fulfillment of the
Requirements for the Degree of

MASTER OF SCIENCE

in the School of Earth and Ocean Science

Parameterizing the breaking and scattering of a mode-1 internal tide on abrupt step topography

by

Emma Christina Murowinski
B.Sc., Acadia University, 2010

Supervisory Committee

Dr. J. Klymak, Supervisor
(School of Earth and Ocean Science)

Dr. P. Cummins, Departmental Member
(School of Earth and Ocean Science)

Dr. J. Scinocca, Departmental Member
(School of Earth and Ocean Science)

Supervisory Committee

Dr. J. Klymak, Supervisor
(School of Earth and Ocean Science)

Dr. P. Cummins, Departmental Member
(School of Earth and Ocean Science)

Dr. J. Scinocca, Departmental Member
(School of Earth and Ocean Science)

ABSTRACT

A parameterization is presented for turbulence dissipation due to baroclinic tide impacting on abrupt shelf topography that is supercritical with respect to the tide. The parameterization requires knowledge of the topography, stratification, and the remote forcing velocity. Upon impact, the tide cascades to higher vertical modes. Vertical internal modes that are arrested at the crest of the topography in the form of lee waves are assumed to dissipate, while faster modes are assumed to propagate away. The energy flux in each mode is predicted with topography that allows linear numerical solutions. The parameterization is tested using high-resolution two-dimensional numerical models of baroclinic tides impinging on an isolated shelf of various heights approximated as a step-function. The recipe is seen to work well compared to numerical simulations of isolated shelves, although it consistently underestimates model flux divergence. Despite low forcing velocities having a more accurate numerical linear solution, the recipe does poorly because it does not accurately predict the modes that become trapped and dissipate. Maximum dissipation occurs when flow is off-shelf and lee waves form, indicating lee waves are the mechanism by which dissipation occurs.

Contents

List of Tables

List of Figures

ACKNOWLEDGEMENTS

My supervisor, Jody for his infinite patience. Ryan, for always being ready to go for coffee and listen to me ramble. Mei, Di, and Jeannette for being awesome office-mates. Sarah and Solomon for being on the other side of the fence. Dylan, Tiegan, Carly, Mallory, Matt, Megan, Kate, Gill, Sarah, and Paul for always being themselves. Feist and Guinevere, for being the sweetest and snuggliest pets a girl could ask for.

DEDICATION

To my parents, Richard and Cathy, for everything.

Chapter 1

Introduction

The creation of baroclinic tides from barotropic tides is believed to be a significant source of mechanical energy that drives the large-scale circulation in the abyssal ocean [Munk and Wunsch, 1998]. The process by which barotropic tides produce internal tides and mixing is sometimes visualized as a cascade from tides to turbulence [Rudnick et al., 2003]. The cascade begins with barotropic tides impacting on topography, such as the Hawaiian Ridge; upon impact, the barotropic tides create baroclinic tides. Internal tides either radiate away from the topography or generate local turbulence. The convergence of surface tidal energy at the Hawaiian Ridge suggests both a divergence of internal tidal energy flux and local dissipation. Klymak et al. [2006] used observations at the Hawaiian Ridge to determine that between 75% and 92% of lost barotropic energy propagates away in the form of low-mode internal tides. The generated internal tides are low mode, high velocity, and low shear, and thus can radiate large distances with minimal interference [Rudnick et al., 2003].

One possible fate of the radiating low-mode internal tide is dissipation on remote topography. Kelly et al. [2013] indicate that mode-1 internal tides can travel uninhibited for 1500 km to 4500 km through the abyssal ocean. Ultimately, the mode-1 tides impact on topography. Although continental slopes are often ineffective generators of internal tides due to barotropic flow being parallel to their prominent bathymetry, this does not rule out their importance as locations of baroclinic tidal dissipation [Nash et al., 2007]. In fact, linear calculations indicate two-thirds of mode-1 tides incident on continental shelves are lost by scattering to higher modes or transmission on shelf [Kelly et al., 2013]. Observations of the Oregon coast by Nash et al. [2007] reveal intense turbulence and elevated dissipation within 500 m of the bottom in regions of rough, abrupt bathymetry, which they attribute largely to low-mode tides.

Steepness is the characteristic of remote topography that dictates the behaviour of radiating low-mode internal tides after impact on said topography. The steepness is defined by the criticality of topography, and is governed by the angle of the slope with respect to the horizontal dh/dx, the stratification of the water $N(z)$, the frequency ω, and the Coriolis frequency f. The criticality of a slope is determined by comparing dh/dx with the aspect ratio of the energy propagation of the internal waves:

$$\beta = \left(\frac{\omega^2 - f^2}{N^2 - \omega^2}\right)^{1/2}.$$

When $\beta > dh/dx$, the slope is considered sub-critical and an incoming internal tide will reflect forewords off the topography and will continue to propagate on-topography. A critical slope occurs when $\beta \approx dh/dx$ and produces turbulent overturns and non-linear breaking events [Eriksen, 1982]. Super-critical topography ($\beta < dh/dx$) allows energy to scatter on topography and continue to propagate over topography, dissipate, as well as reflect back towards the incoming tide. The height of the topography, h_s, determines the size of the surface off which reflection can occur, and by extension controls the fraction of energy reflected. The reflected energy interacts with the incoming tide to set up upward- and downward-travelling beams that radiate away from topographic features. Additional parameters dictate the behaviour of a low-mode tide impacting on a super-critical topography, such as the strength of the mode-1 tide U_0. Mode-1 of the low-mode tide carries most of the energy and influences the fraction of energy that reflects, transmits, and dissipates.

The mechanism that is hypothesized to dominate dissipation at isolated, super-critical topography is trapped lee waves, although observations are still needed for confirmation [Klymak et al., 2013]. Lee waves are generated near the crest of seamounts and continental shelves during each tidal cycle and propagate away as the tide changes. A recipe for parameterizing the dissipation at an isolated super-critical seamount has already been developed and tested against numerical simulations for isolated seamounts [Klymak et al., 2010b, 2013]. The recipe presented in Klymak et al. [2013] explores a low mode internal tide impacting on a Gaussian bump mid-ocean. The recipe predicts dissipation in lee waves by calculating energy flux from linear generation at a knife edge and assuming all modes that move slower than the appropriately averaged ridge-crest speed are arrested and eventually dissipate. Although testing the recipe against numerical simulations showed the parameterization to be reliable, only a small fraction of energy dissipated locally while the rest of the energy radiated away.

Since so much energy escapes supercritical topography, it raises the question where the energy ultimately dissipates. In this thesis, the recipe presented by Klymak et al. [2013] to parameterize mode-1 internal tides is generalized from a knife edge to a step function to emulate idealized continental slope topography. Initially, the numerical model employed will be described (chapter 2) as well as the phenomenology (chapter 3) being explored. The parameterization recipe will then be outlined (chapter 4) and tested against modelled results (chapter 5). Finally the results will be summarized and discussed (chapter 6).

Chapter 2

Numerical Model

The dissipation recipe of Klymak et al. [2013] was tested here against numerical simulations using the Massachusetts Institute of Technology general circulation model (MITgcm) [Marshall et al., 1997], the same model used in numerous two-dimensional wave problems [Klymak et al., 2010b, 2013]. The model used idealized step topography described by

$$h(x) = \begin{cases} -H, & x > 0 \\ -H + h_s, & x < 0 \end{cases}$$

where h_s is the height of the shelf and H is the total water depth. The model was run for varying h_s, summarized in Table 2.1, while H was held constant at $H = 2000\,\mathrm{m}$. The stratification was set to $N_0 = 5.2 \times 10^{-3}\,\mathrm{s}^{-1}$ and the Coriolis frequency was $f = 5.2 \times 10^{-5}\,\mathrm{s}^{-1}$. The model was tidally forced by velocity nudging at the deep-water boundary 500 km from the shelf. On the shelf boundary, a numerical sponge was used to absorb energy that propagated on shelf, eliminating any secondary reflection. The model was run using the hydrostatic approximation for numerical efficiency [Klymak et al., 2013, 2010b].

The dissipation treatment used for the MITgcm simulations in this study follows the scheme presented by Klymak and Legg [2010]. It applies enhanced vertical viscosity and diffusivity in regions of density overturns produced by breaking waves. The diffusivity is scaled by the size of the density overturns, thus energy loss ε is consistent with the Ozmidov scale L_0: $\varepsilon = L_0^2 N^3$. In this case, N is the density-sorted stratification in the overturn. ε is in turn used to determine turbulent viscosity and diffusivitity of $K_\nu = 0.2\varepsilon/N^2$ or $K_\nu = 10^{-5}\,\mathrm{m}^2\,\mathrm{s}^{-1}$, whichever is larger. The dissipation in the scheme must be driven by breaking waves and does not parameterize shear-driven turbulence, which works for our case but is not universally applicable. If the breaking internal waves are small compared to the vertical grid size, the dissipation can remain unresolved. Despite the limitations, comparison with other standard schemes reveal consistent results making the Klymak and Legg [2010] scheme appropriate for the parameter space employed here.

The horizontal and vertical resolutions of the model employed a telescoping coordinate system to both save computational power and resolve the breaking waves. The horizontal resolution, Δx, is 50 m over the shelf-break, and then telescopes to 3500 m over 125 steps to the left of the shelf-break. Right of the shelf break the resolution increases to 200 m for 950 steps and then telescopes back up to 3500 m over the final 125 steps (Figure 2.1a). The same telescoping horizontal resolution is used for all model runs. The vertical resolution, Δz, is spread over 200 steps, and the location of the telescoping changes depending on the shelf height. The finest resolution is 5 m over 100 steps and is centred around the shelf height. On either side of the 100 steps of fine resolution, the resolution scales linearly to 25 m (Figure 2.1b).

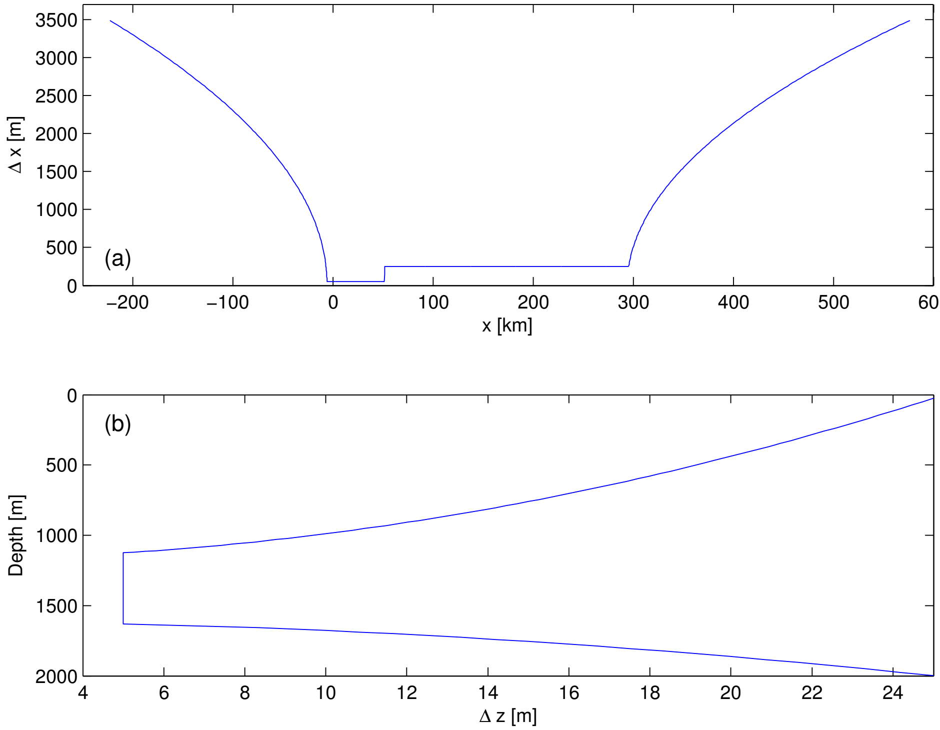

Figure 2.1: (a) The horizontal resolution, Δx plotted against x, and (b) depth plotted against vertical resolution Δz.

H(m)	h_s (m)	U_0 ($\mathrm{m\,s^{-1}}$)	δz (m)	f ($\mathrm{s^{-1}}$)
2000	600	0.04, 0.8, 0.12, 0.18, 0.24	5	5.2×10^{-5}
2000	1010	0.04, 0.8, 0.12, 0.18, 0.24	5	5.2×10^{-5}
2000	1400	0.04, 0.8, 0.12, 0.18, 0.24	5	5.2×10^{-5}

Table 2.1: Summary of model run parameters: H is the total water depth, h_s is the height of the shelf, U_0 is the velocity of the incoming mode-1 tide, δz is the finest vertical resolution, and f is the Coriolis frequency

The model was run for 10 - 20 tidal cycles with baroclinic mode-1 forcing. Three different shelf heights were chosen and the parameters of different model runs are summarized in Table 2.1.

Chapter 3

Phenomenology

We explore a mode-1 internal tide impacting on a continental shelf idealized as a step function. The problem is comprised of three components: an incoming component, a reflected component, and a transmitted component. The mode-1 incoming component propagates towards the shelf (Figure 3.1a). The incoming component hits the continental shelf and scatters into higher modes that reflect and transmit (Figure 3.1b). The reflected component interacts with the incoming component to set up a beam-like standing wave pattern that contains traveling beams radiating away from the shelf, as expected in a super-critical scenario. The lower modes have fully reflected and have set up the basic structure of the standing wave pattern; however, the slower, higher modes have not travelled as far and have only reflected to part-way across the basin (Figure 3.1c). The transmitted component propagates on shelf where the energy contributes to coastal mixing processes. There is no secondary reflection.

3.1 Qualitative Comparison between Analytical and Model Solutions

Modelled results as they approached steady state were compared with a linear analytical solution (Equation 4.1, Equation 4.2, and Equation 4.3), as described in chapter 4. A modelled radiated wave field is faithful to the analytical solution at weak forcing, but less faithful at stronger forcing (Figure 3.2). All comparisons are made for a shelf of $h_s = 1400\,\mathrm{m}$ for 3 different forcing velocities, all scaled by U_0. When U_0 is weak (Figure 3.2a and b) the modelled results and the analytical solution compare well. The higher modes set up a clear, defined beam pattern similar to the pattern

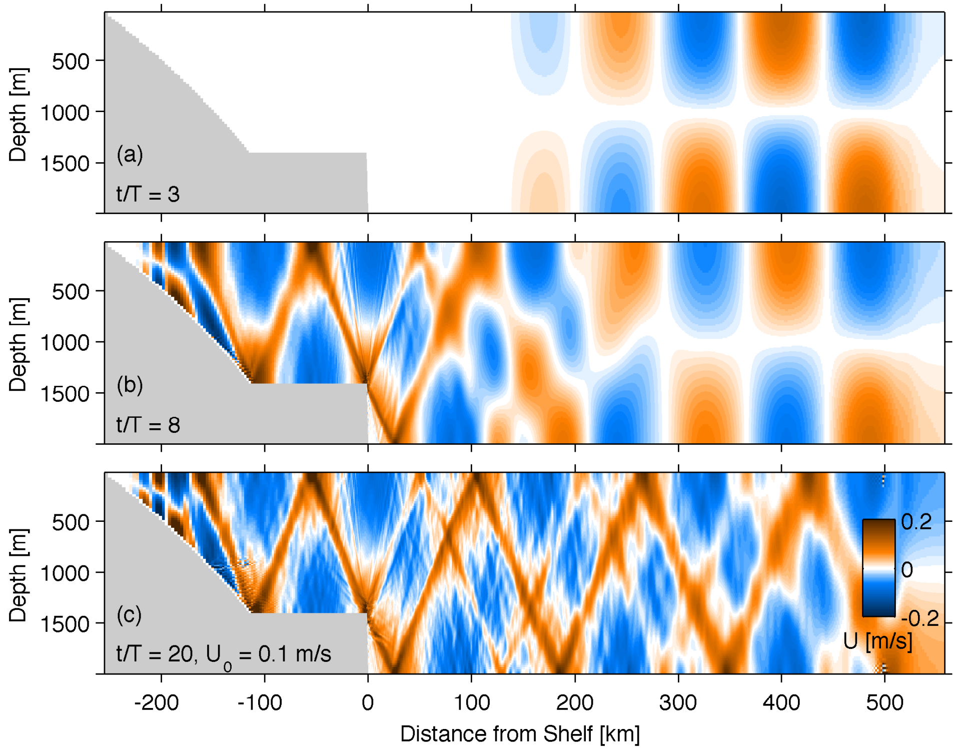

Figure 3.1: (a) The horizontal velocity of a simulated mode-1 internal wave approaches a continental shelf of 600 m at $0.1\,\mathrm{m\,s^{-1}}$, (b) impacts the continental shelf, starting to set up a standing wave pattern. (c) By the 20th tidal cycle the wave pattern is established

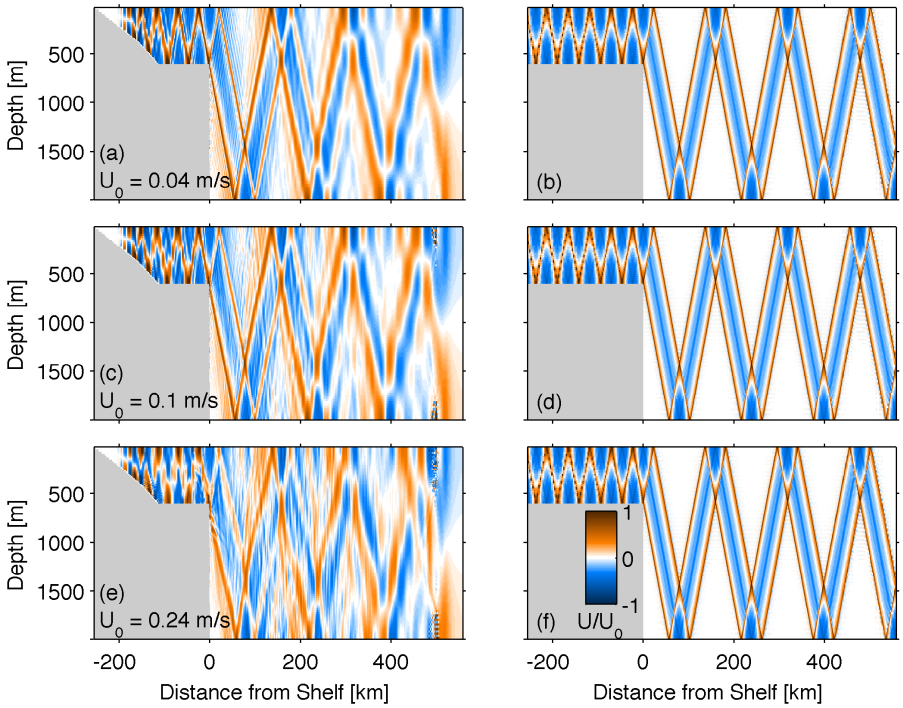

Figure 3.2: Plots of the horizontal velocity normalized by U_0. The left column shows the modelled results and the right column shows the linear analytical results for an incoming wave forced at (a - b) $U_0 = 0.04\,\mathrm{m\,s^{-1}}$, (c - d) $U_0 = 0.10\,\mathrm{m\,s^{-1}}$, and (e - f) $U_0 = 0.24\,\mathrm{m\,s^{-1}}$.

predicted by the analytical solution. The medium U_0 model results also sets up a clear beam pattern; however, the resulting beams are not as well defined as they were for the weaker forcing. Finally, the highest U_0 retains the large-scale features of the analytical solution, but has defocused beams even close to topography.

3.2 Lee Wave Formation

Unlike the analytical solution, the model solution is subject to dissipation; lee waves that form at the shelf break, become trapped, and ultimately dissipate. To effectively illustrate this mechanism, the off-shelf phase of the internal tide interacting with the continental shelf is plotted for the largest forcing velocity, $U_0 = 0.24\,\mathrm{m\,s^{-1}}$ (Figure 3.3). When the flow is dominantly on shelf (blue) the isopycnals are parallel and there is minimal dissipation but there is still a thick mixed layer directly above the shelf break and centred at 1350 m (Figure 3.3a). As the flow changes to off shelf (orange), a hydraulic jump-like feature begins to establish directly above the shelf break (Figure 3.3b - c), as is evident in the isopycnals. A lee wave begins to form at the shelf break (Figure 3.3b). The lee wave is fully formed and turbulent $t/T = 0.3$ tidal cycles after it began to form (Figure 3.3c) and then propagates left as the off shelf flow turns and relaxes (Figure 3.3d).

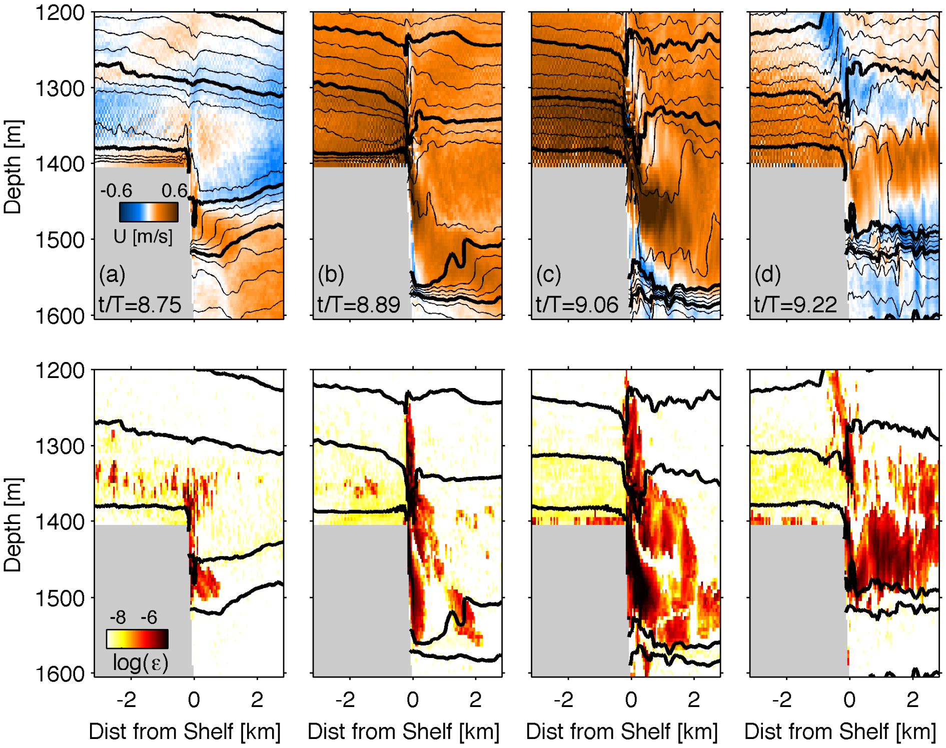

Figure 3.3: The lee wave formation that occurs as the tide turns from dominantly on-shelf (a, blue), to off-shelf (b, orange), on a 600 m shelf forced by $U_0 = 0.24\,\mathrm{m\,s^{-1}}$. As the off shelf flow increases (b - c) the size of the lee wave increases until it begins to propagate off shelf (d) as the tide relaxes. Upper row displays horizontal velocity and lower row displays turbulent dissipation.

During the off-shelf phase of the internal tide (Figure 3.4), the flow is significantly different. Initially the tide is turning and beginning to relax. There is a fully formed turbulent lee wave with a large mixed layer centred around 1400 m and significant dissipation.(Figure 3.4a). As the flow strengthens in the on-shelf direction, the thick low stratification layer becomes less vertical and takes on more of a horizontal shape centred around 1350 m and the amplitude of the lee wave decreases (Figure 3.4b). The large mixed layer and lee wave continue to relax and the dissipation decreases to nearly negligible (Figure 3.4c) until the flow begins to reverse direction again and return to an off-shelf flow (Figure 3.4d). As the flow begins to move off-shelf, the dissipation is still very low and the isopycnals have achieved a nearly horizontal state.

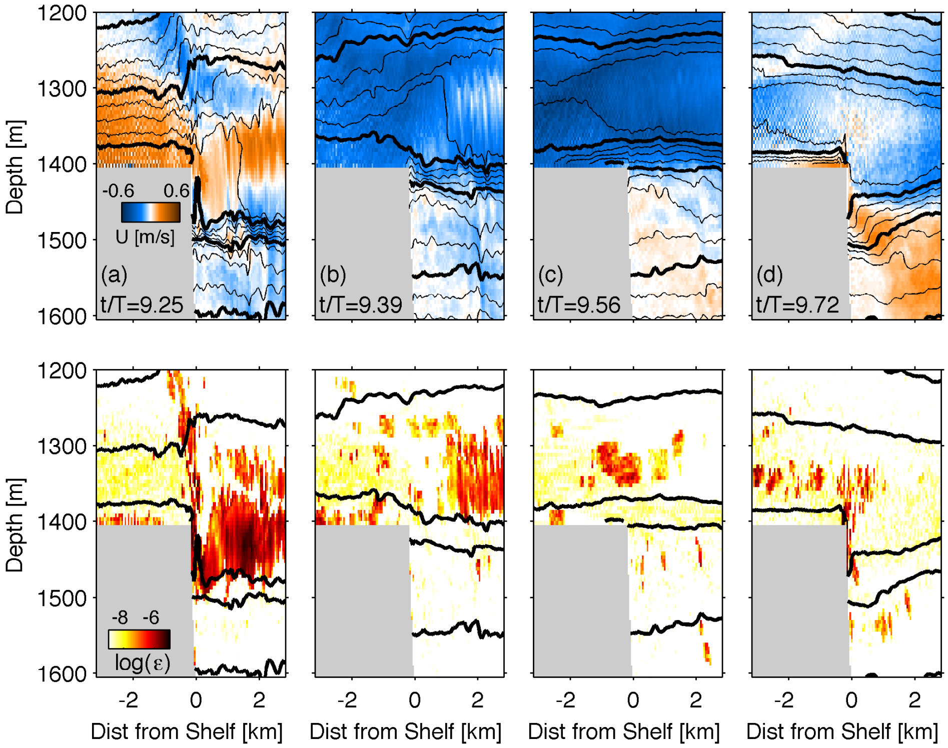

Figure 3.4: The lee wave formation that occurs as the tide turns from dominantly off-shelf (a, blue), to on-shelf (b, orange), on a 600 m shelf forced by $U_0 = 0.24\,\mathrm{m\,s^{-1}}$. As the on shelf flow increases (b-c) the lee waves formed during the previous phase of the tide relax and produce little-to-no dissipation. Upper row displays horizontal velocity and lower row displays turbulent dissipation.

3.3 Dissipation Location

Knowing the location in both space and time of maximum dissipation helps demonstrate the dominance of lee waves as the dissipation mechanism. The dissipation, depth-integrated and averaged over 1 tidal cycle (Figure 3.5a) is at background levels on the shelf. At the shelf-break, the dissipation spikes and then slowly decays to background values off-shelf. Averaged over 1 tidal cycle, the dissipation forms a halo around the shelf-break with the majority occurring at shelf height and slightly off-shelf (Figure 3.5b), supporting dissipation approaching background levels on- and off-shelf. The dissipation was also very time-dependent. The horizontal velocity was averaged 200 m above a 600 m shelf (200 m was chosen because it is the approximate half-wavelength of a lee wave formed under the given conditions; details to follow in chapter 4) and the dissipation was calculated within 6 km on- and off-shelf (Figure 3.6). Maximum dissipation occurred in phase with maximum flow off-shelf at the depth of the shelf break. Dissipation was effectively zero when flow was on-shelf, despite flow being nearly 3 times as strong. As previously illustrated, lee waves only form when flow is off-shelf, thus the maximum dissipation occurring in-phase with weaker flow off-shelf rather than stronger flow on-shelf indicates that the presence of lee waves causes dissipation.

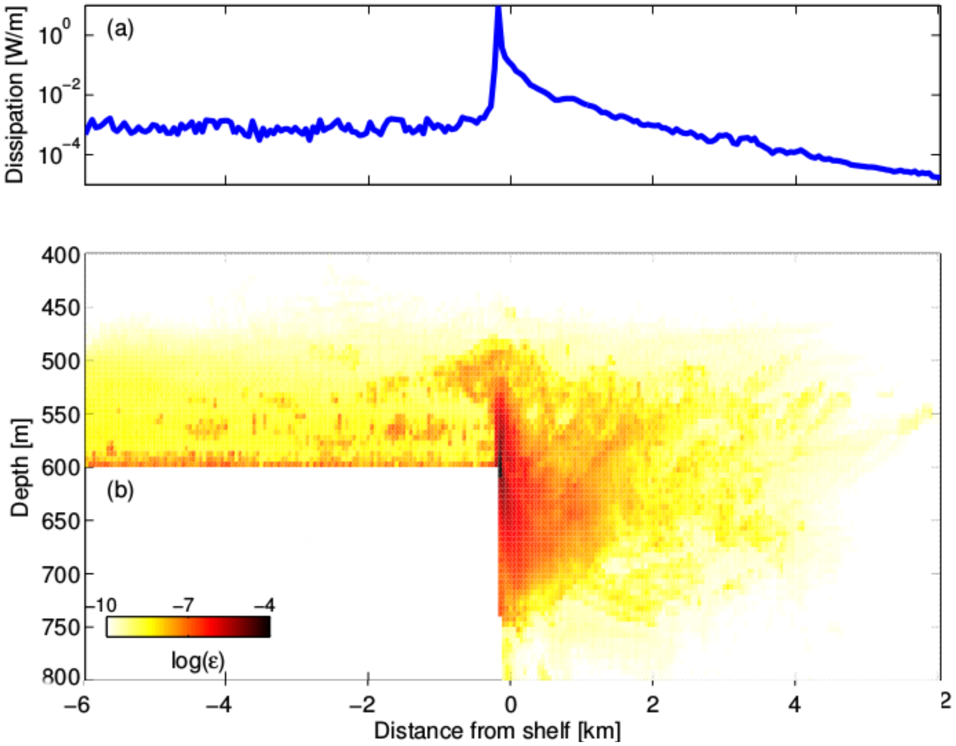

Figure 3.5: The average turbulent dissipation over 1 tidal cycle, shown (a) depth integrated, and (b) over the shelf-break

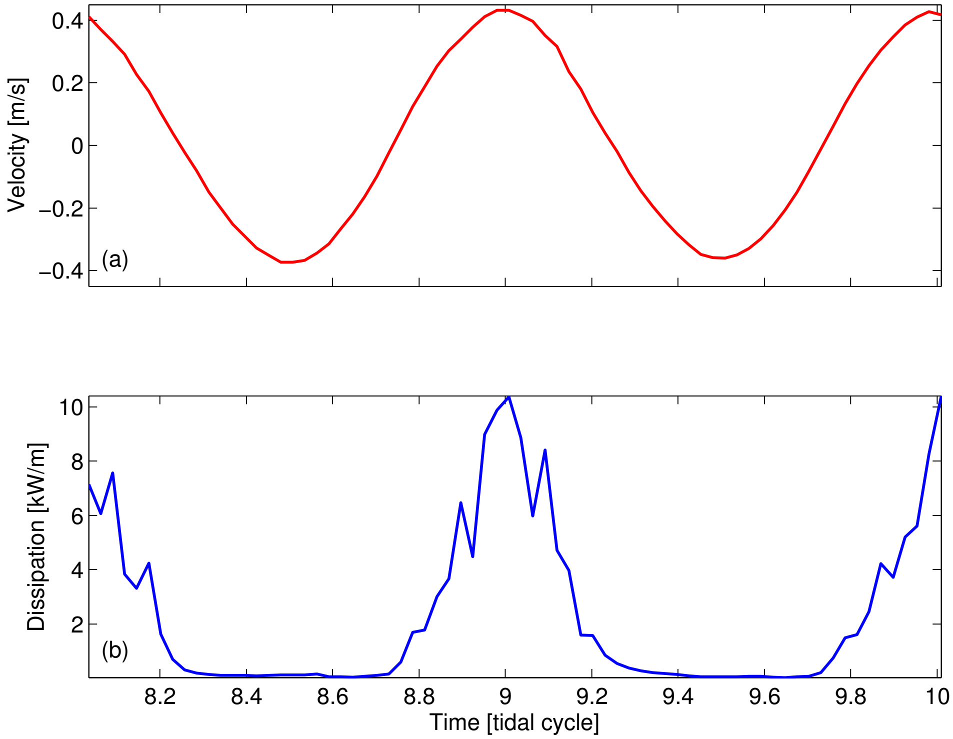

Figure 3.6: (a) The horizontal velocity for a $U_0 = 0.24\,\mathrm{m\,s^{-1}}$ incoming tide averaged at $x = 0$ for 200 m above the 600 m shelf for 2 tidal cycles; (b) turbulent dissipation within 6 km on- and off-shelf for the same 2 tidal cycles.

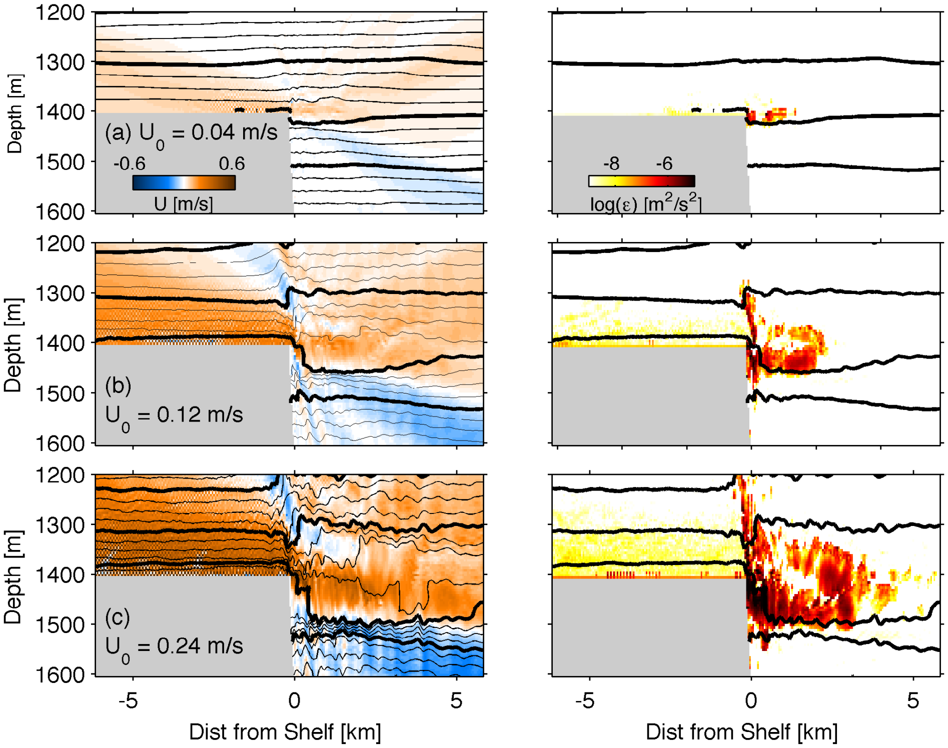

Figure 3.7: The lee wave formation that occurs as the tide turns from dominantly off-shelf (blue), to on-shelf (orange), on to a 600 m shelf with (a) low forcing of $U_0 = 0.4\,\mathrm{m\,s^{-1}}$, (b) medium forcing of $U_0 = 0.12\,\mathrm{m\,s^{-1}}$, and (c) high forcing of $U_0 = 0.24\,\mathrm{m\,s^{-1}}$. The left column of panels show the horizontal velocity and the right column of panels show the corresponding turbulent dissipation.

3.4 Dependence on U_0

The difference in structure of the lee wave is examined for 3 different baroclinic forcings U_0: $0.04\,\mathrm{m\,s^{-1}}$ (low), $0.12\,\mathrm{m\,s^{-1}}$ (medium), and $0.24\,\mathrm{m\,s^{-1}}$ (high) (Figure 3.7). Using a low U_0 forcing produces resulting lee waves that are barely discernible and the isopycnals have minimal movement (Figure 3.7a). There are well defined beams radiating away from the shelf and some minimal dissipation. The medium forcing (Figure 3.7b) results in a lee wave that is larger, implying that more modes and thus more energy are being trapped on shelf to form the lee wave. The deep water still has relatively well-defined beams; however, the beams are thicker, indicating the dominance of a larger vertical wavelength, which is consistent with the trapping of higher modes by turbulence. Finally, the high forcing (Figure 3.7c) has a very large lee wave and thick, poorly-defined radiating beams, therefore continuing to support the concept that only the very low modes radiate off shelf and the rest are trapped and ultimately dissipate.

3.5 Dependence on Shelf Height

The shelf height impacts the size of the produced lee waves and resulting dissipation, with a low shelf producing more dissipation than a high shelf. The difference in velocity and lee wave formation for the three different shelf heights are all shown, with the same colour axis and the same U_0 (Figure 3.8). The lowest shelf height (Figure 3.8a) results in the highest local velocity at the shelf break ($0.19\,\mathrm{m\,s^{-1}}$) that produces the largest lee waves. As discussed earlier, a large lee wave corresponds to a high dissipation, as is demonstrated by the dissipation plot. A large lee wave is caused by lower modes carrying more energy being arrested, thus the dissipation from a large lee wave includes more energy. As the shelf height increases (Figure 3.8b), the local velocity at the shelf break ($0.14\,\mathrm{m\,s^{-1}}$) and size of the lee wave decreases as does the dissipation. The higher shelf heights have a larger reflected surface for the incoming energy, so the beams radiating away from the shelf are more defined and focused, again indicating more energy escaping. It is readily apparent that the highest shelf height (Figure 3.8c) has the weakest local velocity ($0.06\,\mathrm{m\,s^{-1}}$) that produces smallest lee waves and lowest dissipation. The high shelf provides a large surface against which the incoming energy can reflect with minimal dissipation, leading to the slim, well defined beams.

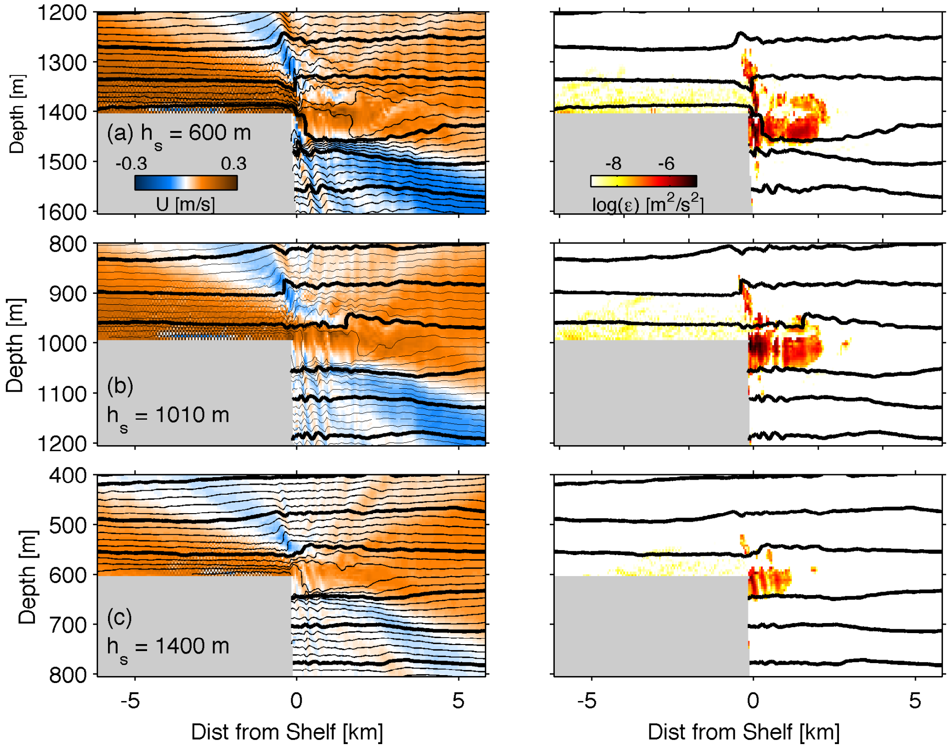

Figure 3.8: The lee wave formation that occurs as the tide turns from dominantly off-shelf (blue), to on-shelf (orange), when a mode-1 wave of $U_0 = 0.12\,\mathrm{m\,s^{-1}}$ impacts the shelf. The local velocity 200 m above each shelf height is very different: (a) a low 600 m shelf has a local velocity of $0.19\,\mathrm{m\,s^{-1}}$ (b) a medium 1010 m shelf has a local velocity of $0.14\,\mathrm{m\,s^{-1}}$, and (c) a high 1400 m shelf has a local velocity of $0.06\,\mathrm{m\,s^{-1}}$. The left column of panels show the horizontal velocity and the right column of panels show the corresponding turbulent dissipation.

3.6 Steady State

To enable comparison between the analytical solution and the model results in steady state, the model results are examined to determine when they achieve steady state. A mode-1 tide approaches the shelf carrying significant energy flux (Figure 3.9a). Upon impact, the energy scatters into many modes that reflect back into the basin at different velocities. The reflected low modes are faster and interfere with the incoming mode-1 flux first; thus, when averaged over a tidal cycle the net flux is significantly less than the original incoming flux (Figure 3.9b). As time progresses, lower modes also propagate across the basin such that the next flux is effectively constant and thus in steady state. In addition to the flux setting up a steady state, the dissipation also sets up a steady state. Immediately after impacting the shelf, the initial scattering produces a tidal cycle of maximum dissipation (Figure 3.10). Within a few tidal cycles, the solution begins to form and the dissipation is constant with time, and remains constant from the 8th to the 14th tidal cycle. After the 14th tidal cycle the dissipation decays further due to stratification being mixed and the solution achieving a more steady energy balance and a more fully formed solution. In future calculations when values over a single tidal cycle are required, the measurements will be from the 9th tidal cycle. The 9th tidal cycle is a good choice because the initial period of high-dissipation has passed, but mixing has not caused the initial stratification to decay extensively.

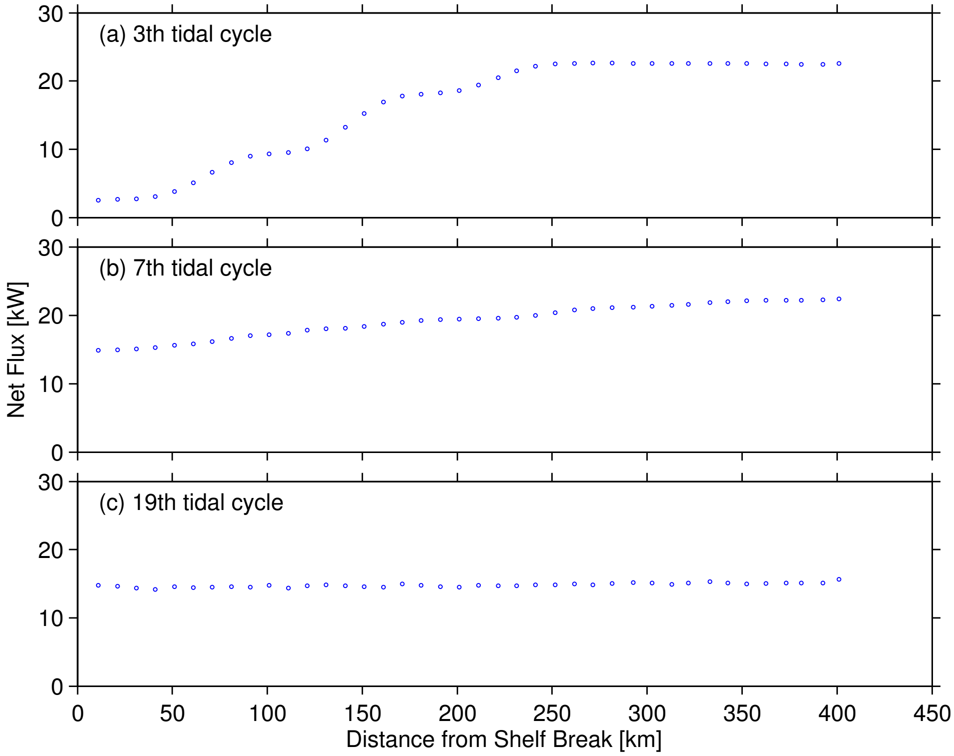

Figure 3.9: Net energy flux of a $U_0 = 0.12\,\mathrm{m\,s^{-1}}$ incoming tide impacting a 600 m shelf averaged over a tidal cycle plotted against distance off-shelf from shelf break, averaged over the (a) 3rd, (b) 7th, and (c) 19th tidal cycle.

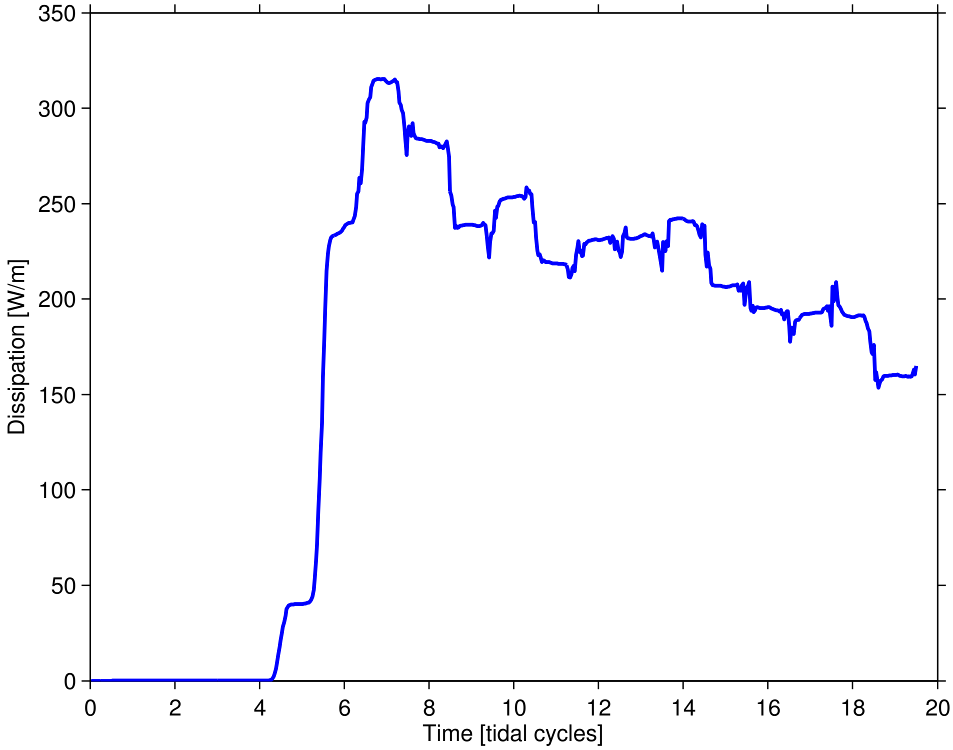

Figure 3.10: The dissipation calculated within 6 km on- and off-shelf of a 600 m shelf impacted by a $U_0 = 0.12\,\mathrm{m\,s^{-1}}$ tide, smoothed over 2 tidal cycles.

Chapter 4

Parameterization

Similar to Klymak et al. [2010b] and Klymak et al. [2013], the parameterization for turbulence dissipation at an isolated supercritical topography assumes that reflected and transmitted vertical modes with a horizontal speed faster than the baroclinic velocity at the slope-crest escape, while other modes are arrested and dissipate locally.

To formulate the recipe, we follow a geometric approach, parallel to Klymak et al. [2013, 2010b] and St. Laurent et al. [2003]. In the absence of a barotropic forcing, the flow is decomposed into 3 baroclinic waves: an incident wave, u_i, a reflected wave, u_r, and a transmitted wave, u_t (Figure 4.1). The ocean is stretched via a WKB (Wentzel-Kramers-Brillouin) co-ordinate transform to a constantly stratified ocean. The coordinate transform is normalized such that $H = \hat{H}$ is the depth of the ocean basin and the shelf depth is $\hat{h}_s = \int_{h_s}^{0} \frac{N(z)}{N_0} dz$, where $N(z)$ is the stratification, N_0 is the buoyancy frequency, and $\hat{h}_s$ is the depth of the ocean above the shelf.

Each wave can then be described as a sum of n vertical modes. Vertical modes isolate the vertical structure of internal waves and are formed from the equations of motion by separation of variables. They must obey the eigenvalue problem in the vertical

$$\frac{d^2\phi(z)}{dz^2} + \frac{N^2}{c_e^2}\phi(z) = 0$$

where $\phi(z)$ is the vertical signal being decomposed into modes and c_e are the eigenvalues. Boundary conditions are imposed at the sea surface and sea floor such that $d\phi/dz(z = 0) = d\phi/dz(z = -H) = 0$ and the eigenvalue problem has orthogonal solutions that allow the flow to be broken down into discrete vertical modes [Kundu,

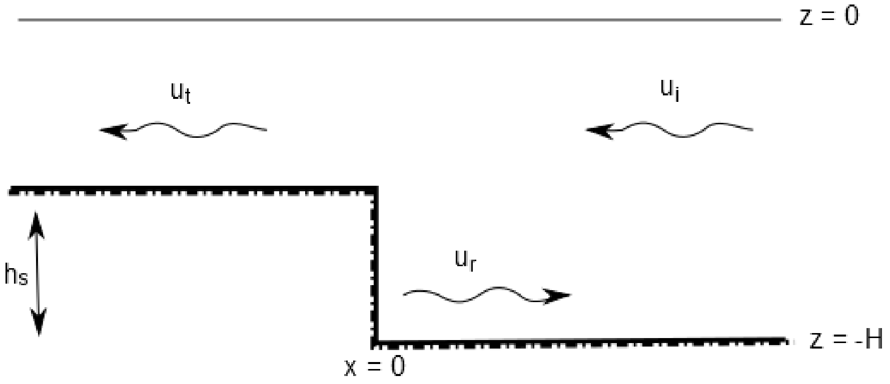

Figure 4.1: Schematic describing the essential elements of the parameterization, including the incident wave (u_i), reflected wave (u_r), and transmitted wave (u_t).

1990]. The solution for $\phi(z)$ must therefore have the vertical structure

$$\phi_n(z) = \cos\left(\frac{\pi n z}{H}\right)$$

where n is an integer that indicates the vertical mode and $\phi_n(z)$ is the vertical structure of the n^{th} mode of $\phi(z)$.

The velocities must obey the continuity equation, therefore

$$u_t = u_i + u_r, z > -h$$

$$0 = u_i + u_r, -H < z < -h$$

$$w_t = w_i + w_r, -H < z < 0$$

where w_i, w_r and w_t are the vertical velocities of the incoming, reflected, and transmitted wave, respectively.

By following Klymak et al. [2011] (similar to St. Laurent et al. [2003]), the coupled set of equations is achieved and solved for $a_i(n)$, the amplitude of the incoming component, $a_r(n)$, the amplitude of the reflected component, and $a_t(n)$, the amplitude of the transmitted component, using l, m, and n as mode indices

$$a_i(m) + a_r(m) = \mathbf{A}(m,n)a_t(n)$$

$$a_t(n) = \mathbf{B}(n,l)[a_r(l) - a_i(l)]$$

which are then solved for $a_r(m)$

$$a_r(m) = (\mathbf{A}(m,n)\mathbf{B}(n,l) - \mathbf{I}(m,l))^{-1}(\mathbf{A}(m,n)\mathbf{B}(n,l) + \mathbf{I}(m,l))a_i(l)$$

and $a_t(n)$

$$a_t(n) = \mathbf{B}(n,l)(a_r(l) - a_i(l))$$

where $\mathbf{A}(m,n)$ and $\mathbf{B}(n,l)$

$$\mathbf{A}(m,n) = \frac{2m\gamma^2(-1)^n \sin(m\pi\gamma)}{\pi[m^2\gamma^2 - n^2]}$$

$$\mathbf{B}(n,l) = \frac{2n(-1)^2 \sin(l\pi\gamma)}{\pi[n^2 - l^2\gamma^2]}$$

and $\gamma = \hat{h}_s/\hat{H}$ and $\mathbf{I}(m,l)$ is the identity matrix.

Now that we have the amplitudes of the waves as a function of mode, we can describe the three waves in our problem as

$$\hat{u}_i = Re\left\{\sum_n a_i(n)\cos\left(\frac{n\pi\hat{z}}{\hat{H}}\right)e^{i(k_n x-\omega t)}\right\} \tag{4.1}$$

$$\hat{u}_r = Re\left\{\sum_n a_r(n)\cos\left(\frac{n\pi\hat{z}}{\hat{H}}\right)e^{i(k_n x+\omega t)}\right\} \tag{4.2}$$

$$\hat{u}_t = Re\left\{\sum_n a_t(n)\cos\left(\frac{n\pi\hat{z}}{\hat{h}_s}\right)e^{i(k_n^s x-\omega t)}\right\} \tag{4.3}$$

The coefficients, $a_i(n)$, $a_r(n)$, and $a_t(n)$ are complex to accommodate the different phases of the waves with respect to each other when they arrive at the continental shelf. $k_n = \alpha n\pi/\hat{H}$ and $k_n^s = \alpha n\pi/\hat{h}_s$ are the horizontal wavelengths in the deep basin and shelf, respectively. The three waves are then used to calculate the energy flux as a function of mode number (Appendix section A.3), resulting in the equations

$$F_i(n) = \hat{H}\frac{g(\omega)}{m(n)}\frac{a_i^2(n)}{4} \tag{4.4}$$

$$F_r(n) = \hat{H}\frac{g(\omega)}{m(n)}\frac{a_r^2(n)}{4} \tag{4.5}$$

$$F_t(n) = \hat{h_s}\frac{g(\omega)}{m(n)}\frac{a_t^2(n)}{4} \tag{4.6}$$

where $F_i(n)$, $F_r(n)$, and $F_t(n)$ are the incoming, reflected, and transmitted energy as a function of n, $m(n) = n\pi/\hat{H}$ and

$$g(\omega) = \rho\frac{[(N_0^2-\omega^2)(\omega^2-f^2)]^{1/2}}{\omega}.$$

We now want to know what modes have a horizontal velocity slower than the velocity at the shelf crest and will be trapped, form lee waves, and dissipate. A procedure parallel to Klymak et al. [2013] is employed. The linear solution for the total velocity at the shelf break is calculated by summing the lower modes up to an arbitrary cutoff of M

$$u_M(z,t) = \sum_{n=0}^{M} a(n)\phi_n(z)e^{i(k_n x - \omega t)}$$

where $a(n) = a_t(n)$ for the on shelf solution and $a(n) = a_r(n) + a_t(n)$ for the off shelf solution. The cumulative velocity $u_M(z,t)$ is then averaged over half a vertical wavelength of the M^{th} critical mode $\lambda_M = H/M$ and the maximum over a tidal cycle is chosen

$$U_M = \max\left(\langle u_M(z,t)\rangle_{z=-H+h_s}^{-H+h_s+\lambda_M}\right)_{tide} \tag{4.7}$$

Klymak et al. [2013] shows the lee wave to be on the order of half a vertical wavelength of the arrested mode, which is the motivation for the vertical averaging scale. Since the critical mode is unknown, U_M is calculated and compared with c_M, the eigen speed of the M^{th} mode

$$c_M = c_e(M) = \frac{NH}{M\pi}. \tag{4.8}$$

The critical mode is then chosen to be the lowest mode where $c_M \le U_M$. In the hydrostatic nonrotating limit the eigen speed is equal to the phase and group speed of lee waves because $\omega_{lee} >> f$. The hydrostatic tidal-frequency phase speed relates to the eigen speed by $c_p = c_n\omega/(\omega^2 - f^2)^{1/2}$ thus the eigen speed can be used to choose the critical mode without changing the results [Klymak et al., 2010b].

It is important to note that this procedure must be performed twice: once for on shelf velocities by calculating u_M using $a(n) = a_t(n)$ and providing a critical mode M_t, once for off shelf velocities by calculating u_M using $a(n) = a_i(n) + a_r(n)$ resulting in a critical mode M_r. From the critical mode, which is the lowest arrested mode, the dissipation, D, is easily calculated as

$$D = \sum_{n=M_t}^{\infty} F_t(n) + \sum_{n=M_r}^{\infty} F_r(n) \tag{4.9}$$

where $F_r(n)$ and $F_t(n)$ is the energy predicted to be put into each mode of the reflected and transmitted components, respectively.

To summarize, in this recipe

1. determine the linear response due to forcing represented by the modal amplitudes $a_i(n)$, the coefficients $a_t(n)$, $a_r(n)$, and the energy fluxes $F_t(n)$ and $F_r(n)$;

2. iterate through all modes M to determine a velocity scale at the top of the shelf, in the deep and shallow water U_M;
3. the lowest mode with eigenspeed slower than the corresponding U_M (i.e., $c_r \leq U_M$, in the deep water) is chosen as the critical mode in the deep and shallow water;
4. the dissipation is the sum of energy put into modes M and higher: $D = \sum_{n=M}^{\infty} F_r(n) + F_t(n)$

Chapter 5

Results

The energy budget for the shelf system is calculated 6 km on- and off-shelf. The energy source for the system is the incoming mode-1 baroclinic tide (F_i) that is forced remotely via velocity nudging. The incoming energy scatters into modes at the shelf break. Energy reflects and transmits in the form of baroclinic (F_r and F_t, respectively) and barotropic ($F_{r,BT}$ and $F_{t,BT}$, respectively) energy. A small fraction of the incoming energy does not escape as reflected or transmitted energy and dissipates at the shelf-break. The amount of energy that does not escape is the flux divergence (F_{diverg}). The energy terms in the system can be summarized as

$$F_{diverg} = (F_i + F_r + F_{r,BT}) - (F_t + F_{t,BT}).$$

In the deep, off-shelf water the incoming and reflected energy flux interfere such that the flux calculated directly from the mode is the net flux (F_d). The flux divergence is calculated from the net flux in the deep and shallow water 6 km on- and off-shelf:

$$F_{diverg} = (F_d + F_{d,BT}) - (F_t + F_{t,BT}).$$

When calculating the energy budget from the model, the net velocity of the baroclinic tide on- and off-shelf was decomposed into mode components. Since all incoming baroclinic energy is in mode 1, the mode-1 net velocity off-shelf was separated into an incoming and outgoing component. When separating into the incoming and outgoing component, a time series over 2 tidal cycles is fit by an ellipse. Depending on the strength of the incoming velocity U_0 and the shelf height, the ellipse fit to the time series can be very good or poorer. A good fit occurs when all the values in the time series fit tightly to the ellipse, and a poor fit occurs when the ellipse requires a lot of approximations and many time series values do not fall on the ellipse. The incoming, reflected, and transmitted baroclinic flux was then calculated from the separated and decomposed velocities (Table 5.1, Appendix A).

The barotropic flux is a minor energy sink for the incoming mode-1 baroclinic energy. The reflected and transmitted barotropic flux accounts for less than 1 % of the incoming baroclinic energy (Figure 5.1). For each shelf-height, the percentage of barotropic flux is consistent and dependent on the height of the shelf, rather than the forcing. In the shallow water above a 600 m shelf, the barotropic energy flux sinks less than 0.05 % of the incoming energy. The the barotropic flux in the shallow water on-shelf for a medium 1010 m shelf sinks at most 0.08 %, and for a high 1400 m shelf approximately 0.02 % (Figure 5.1). In the deep water off-shelf, the barotropic tide also sinks a small percentage of the incoming baroclinic energy: 0.95 % for a 1400 m shelf, 0.6% for a 1010 m shelf, and 0.25 % for a 600 m shelf.

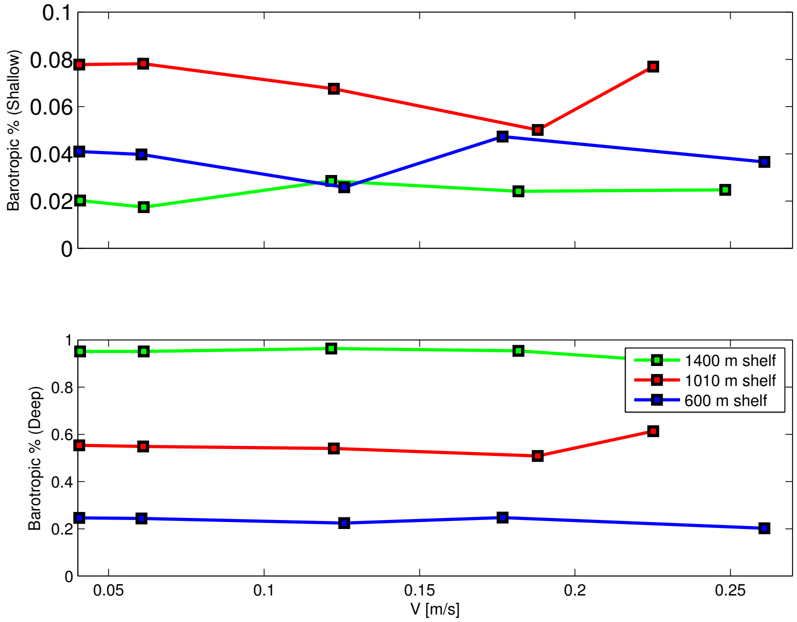

Figure 5.1: (a) The percentage of net energy in the shallow water 6 km on-shelf that is in the form of barotropic energy averaged over the 9th tidal cycle, and (b) the percentage of net energy in the deep water 6 km off-shelf that is in the form of barotropic energy averaged over 9th tidal cycle.

The baroclinic flux calculated from the linear solution agrees with the baroclinic flux produced by the numerical model results. The flux for the incoming, reflected,

Table 5.1: Summary of the energy budget of the system for each shelf height and forcing velocity. All fluxes are calculated 6 km on- and off-shelf during the 9th tidal cycle. Note that the flux divergence (F_{diverg}) is calculated from the net flux 6 km in the deep water, not the incoming and reflected flux.

h_s [m]	$U_0 [\mathrm{m\,s^{-1}}]$	F_d ($F_{d,BT}$) [$\mathrm{kW\,m^{-1}}$]	F_t ($F_{t,BT}$) [$\mathrm{kW\,m^{-1}}$]	F_{diverg}	D_{model}	D_{param}
1400	0.25	4.48 (-0.87)	3.19 (-0.02)	0.44	0.51	0.38
1400	0.18	2.64 (-0.50)	1.86 (-0.01)	0.30	0.20	0.14
1400	0.12	1.15 (-0.22)	0.85 (-0.01)	0.07	0.06	0.05
1400	0.06	0.29 (-0.06)	0.22 (-0.00)	0.01	0.01	0.01
1400	0.04	0.13 (-0.03)	0.10 (-0.00)	0.01	0.00	0.00
1010	0.23	22.63 (-0.49)	19.10 (0.06)	2.98	2.15	1.06
1010	0.19	12.64 (-0.28)	11.07 (0.03)	1.26	0.83	0.67
1010	0.12	5.59 (-0.13)	5.06 (0.02)	0.38	0.23	0.18
1010	0.06	1.38 (-0.03)	1.29 (0.00)	0.05	0.03	0.02
1010	0.04	0.61 (-0.01)	0.58 (0.00)	0.02	0.01	0.01
600	0.26	57.48 (-0.22)	53.79 (0.04)	3.43	2.24	2.48
600	0.18	32.05 (-0.12)	30.47 (0.02)	1.43	0.95	0.72
600	0.13	14.20 (-0.06)	13.66 (0.01)	0.47	0.30	0.26
600	0.06	3.53 (-0.01)	3.45 (0.00)	0.07	0.03	0.03
600	0.04	1.57 (-0.01)	1.54 (0.00)	0.02	0.01	0.01

and transmitted components can all be calculated using the linear solution to the step function problem (Equation 4.4, Equation 4.5, and Equation 4.6). We compare the modelled energy flux averaged over the 9th tidal cycle 6 km on- and off-shelf to the linear solution for all three shelf-heights: $1400\,\mathrm{m}$, $1010\,\mathrm{m}$, and $600\,\mathrm{m}$ (Figure 5.2, Figure 5.3, and Figure 5.4, respectively). When the mode number is low, the flux calculated from the linear solution is a very good estimate of the model flux, regardless of shelf height or forcing velocity. As mode number increases, the linear solution provides an increasingly poor estimate of flux for all U_0. The linear solution is in steady state and assumes no dissipation, whereas the model undergoes dissipation and as mode number increases the flux falls away from the linear solution. The flux drop off is at higher modes, indicating that they are dissipated. As forcing increases, lower modes drop off and thus more modes are dissipated. The strongest forcings fall away from the linear solution at the lowest modes and have a low cutoff mode. The weakest forcings have the least dissipation and a very high mode cutoff,and thus follow the linear solution very well.

The iterative procedure to determine the cutoff mode from the parameterization recipe will be illustrated step-by-step. The procedure is designed to predict the critical mode where higher modes are arrested at the shelf-break and dissipate, while lower modes escape and propagate away. An example profile is considered for a ridge height of 600 m and $U_0 = 0.12\,\mathrm{m\,s^{-1}}$ (Figure 5.5). All modes summed together (red lines, which are the same in all panels) have an abrupt maximum as the top of the shelf and then experience a zero crossing approximately 400 m above the shelf. If a critical mode of $M = 10$ is chosen (Figure 5.5a), $c_{10} = 0.33\,\mathrm{m\,s^{-1}}$ (black dashed line) and the profile of U_{10} (blue curve) is only composed of the first 10 modes. The mean of the $M = 10$ line for a half wavelength above the ridge crest is less than c_{10}: $U_{10} = 0.17\,\mathrm{m\,s^{-1}}$. Thus, mode 10 is not critical and can propagate away from the shelf in the reflected direction. When the same procedure is applied to $M = 16$ and $M = 20$, both are too high, but $M = 15$ is critical. If the incoming mode-1 tide is stronger in amplitude, there is a corresponding drop is in critical mode as amplitude increases (Figure 5.6). The same procedure must be applied to the shallow water to determine the critical mode for the transmitted wave.

The dissipation was calculated from the recipe for 3 different shelf heights and 5 different forcing velocities each (Table 2.1). The model dissipation was also calculated from the model for shelf height and forcing velocity using two different methods. The first method was to calculate dissipation by determining the flux divergence, or

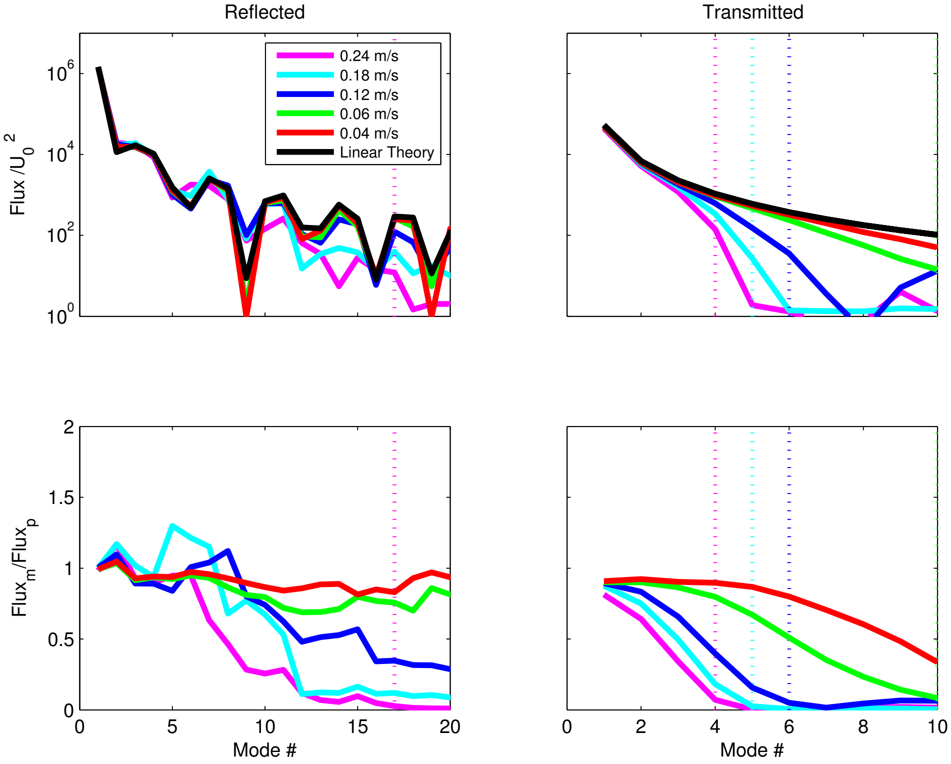

Figure 5.2: Energy flux averaged over the 9th tidal cycle for a shelf of 1400 m. Left column shows the reflected flux 6 km off-shelf, and right column shows the transmitted flux 6 km on-shelf. Top shows flux normalized by U_0^2 and the bottom shows the ratio between the modelled and parameterized flux. Note that the bottom plots are smoothed over 3 modes; however the upper plots are not smoothed.

rather the difference in net incoming and outgoing fluxes. The second method was to determine dissipation was by integrating the dissipation values over the shelf-break calculated by the model using the numerical dissipation scheme. The numerical dissipation scheme is employed because it allows turbulent dissipation calculations without requiring direct numerical simulations. Numerical simulations of dissipation are prohibitively computationally expensive. The two methods for calculating dissipation values from the model yielded different results; the values calculated from the flux divergence were significantly lower (Table 5.1). The advection scheme employed by the model is noisy, and some of the noise produces extra dissipation in the dissipation scheme calculations. A finer vertical model resolution allows significant noise to develop due to inaccuracies in the advection scheme producing more overturns, thus calculated dissipation values are too high [Klymak and Legg, 2010]. We have

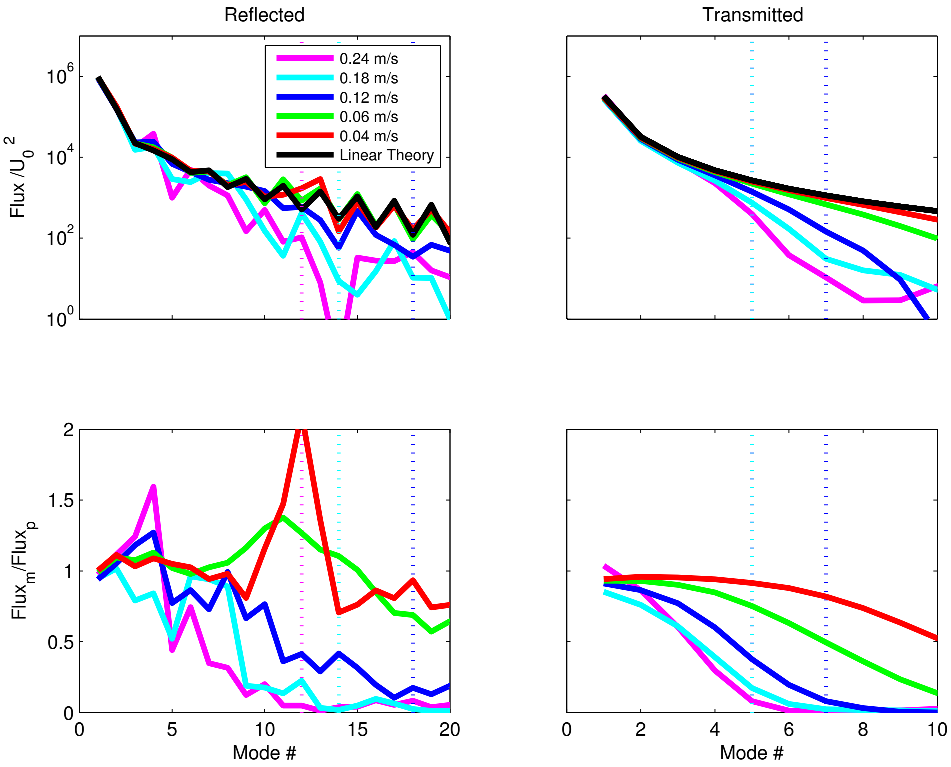

Figure 5.3: Energy flux averaged over the 9th tidal cycle for a shelf of 1010 m. Left column shows the reflected flux 6 km off-shelf, and right column shows the transmitted flux 6 km on-shelf. Top shows flux normalized by U_0^2 and the bottom shows the ratio between the modelled and parameterized flux. Note that the bottom plots are smoothed over 3 modes; however the upper plots are not smoothed.

more confidence in the dissipation values calculated from flux divergence because the method employed is a more direct calculation of the energy loss over the shelf.

The dissipation predicted by the recipe (D_{param}) agrees very well with the dissipation calculated directly from the two-dimensional numerical model results (D_{model}, Figure 5.7, small squares). The underestimation of dissipation by the recipe indicates that the recipe does not chose critical modes low enough and more modes are being dissipated in the model than are being dissipated by the recipe. Figure 5.2, Figure 5.3 and Figure 5.4 all show that at strong forcing velocities (pink, cyan, and blue) the recipe's chosen cutoff mode (the horizontal dotted line) occurs at a higher mode than the mode at which the visible flux roll-off occurs. At low dissipations the recipe begins to significantly under predict the flux divergence. The flux divergence approaches minimal background dissipation values, whereas the recipe and direct model dissipa-

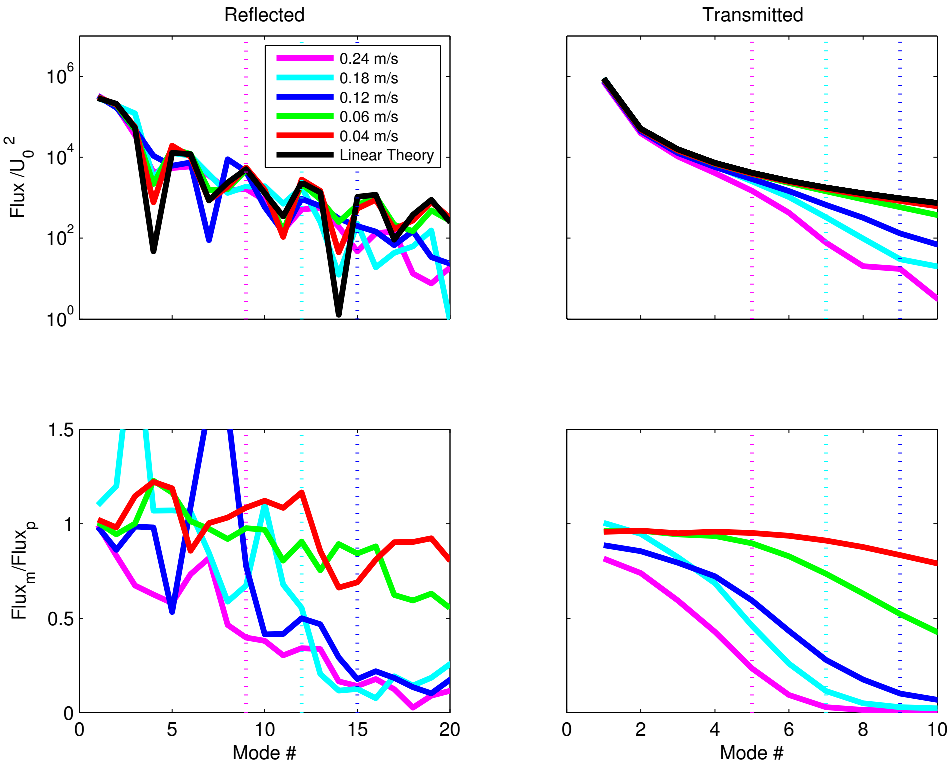

Figure 5.4: Energy flux averaged over the 9th tidal cycle for a shelf of 600 m. Left column shows the reflected flux 6 km off-shelf, and right column shows the transmitted flux 6 km on-shelf. Top row shows flux normalized by U_0^2 and the bottom row shows the ratio between the modelled and parameterized flux. Note that the bottom plots are smoothed over 3 modes; however the upper plots are not smoothed.

tion results do not encounter such a physically limiting factor. The recipe, and to a lesser extent the direct model dissipation results, continue to predict smaller and smaller dissipation values. Note that the dissipation in both the parameterization and the model scales with U_0^3 (Figure 5.8), allowing comparison of model runs with a range of forcings on the almost-collapsed curve.

Motivation for exploring the parameterization came from a desire to understand contributions to deep ocean mixing. A very small percentage of incoming flux is dissipated at the shelf-break (Figure 5.9); even at the strongest U_0, when $U_0 = 0.28\,\mathrm{m\,s^{-1}}$, less than 3% of the incoming energy is dissipated. Both a 600 m shelf and a 1010 m shelf have dissipation that scales linearly from less than 0.5% at the lowest forcing of $U_0 = 0.04 m/s$ to $2 - 3\%$ at the strongest forcing of $U_0 = 0.28\,\mathrm{m\,s^{-1}}$ (Figure 5.9).

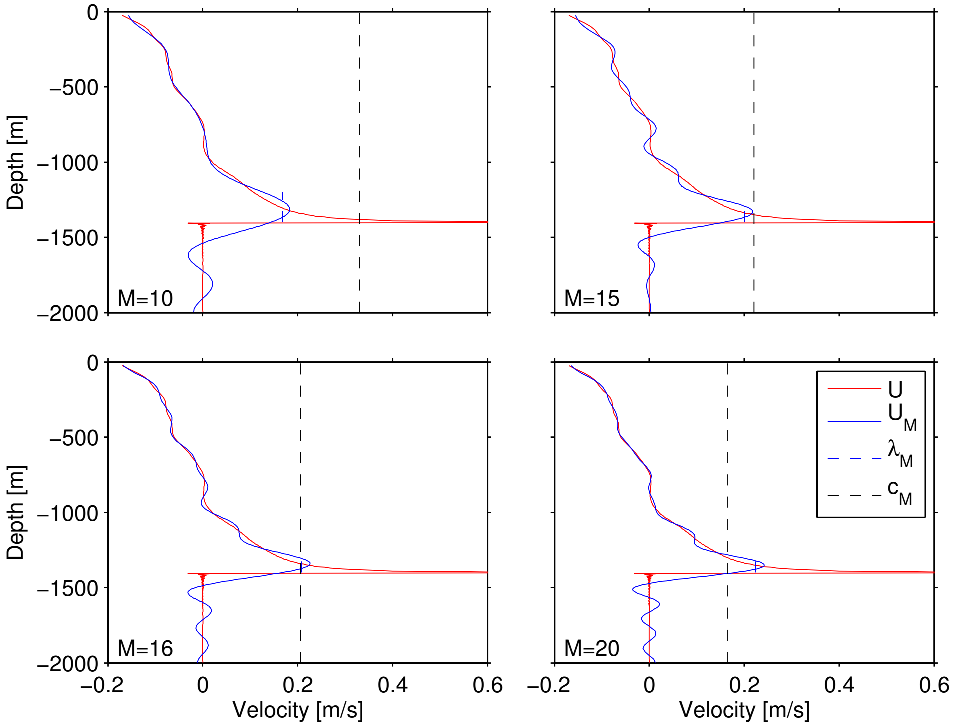

Figure 5.5: Example of off-shelf iterations to chose a critical mode, such that the phase speed of the mode is slower than the flow speed due to all lower modes. The red line shows the total modelled velocity at the shelf-break, the blue line shows the sum of modes 1 to M, the black dashed line shows c_M, or rather the mean speed over half the wavelength of the M^{th} mode, and the blue dashed line is the phase speed of the M^{th} mode. Note that the length of the blue dashed line also shows the length of the half wavelength of the M^{th} mode.

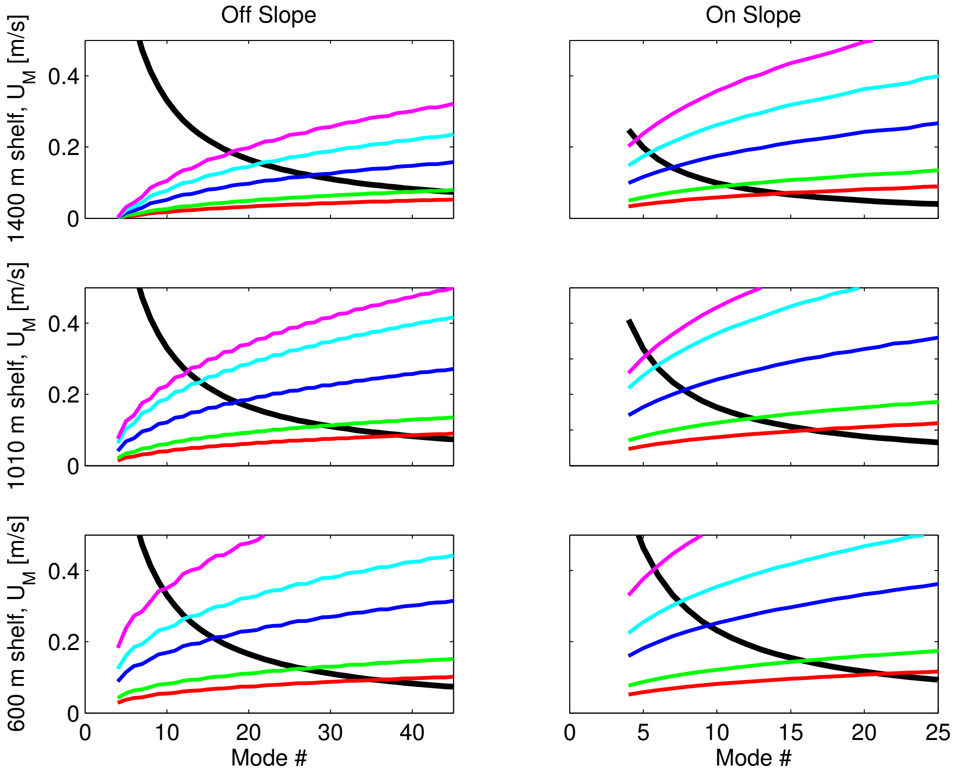

Figure 5.6: U_M for 5 different forcing velocities compared with c_M for that depth of ocean. Left column shows the results off shelf and right column shows the results on shelf. The top row shows the results for a shelf of 1400 m, the middle row shows the results of a shelf of 1010 m, and the bottom row shows the results of a shelf of 600 m.

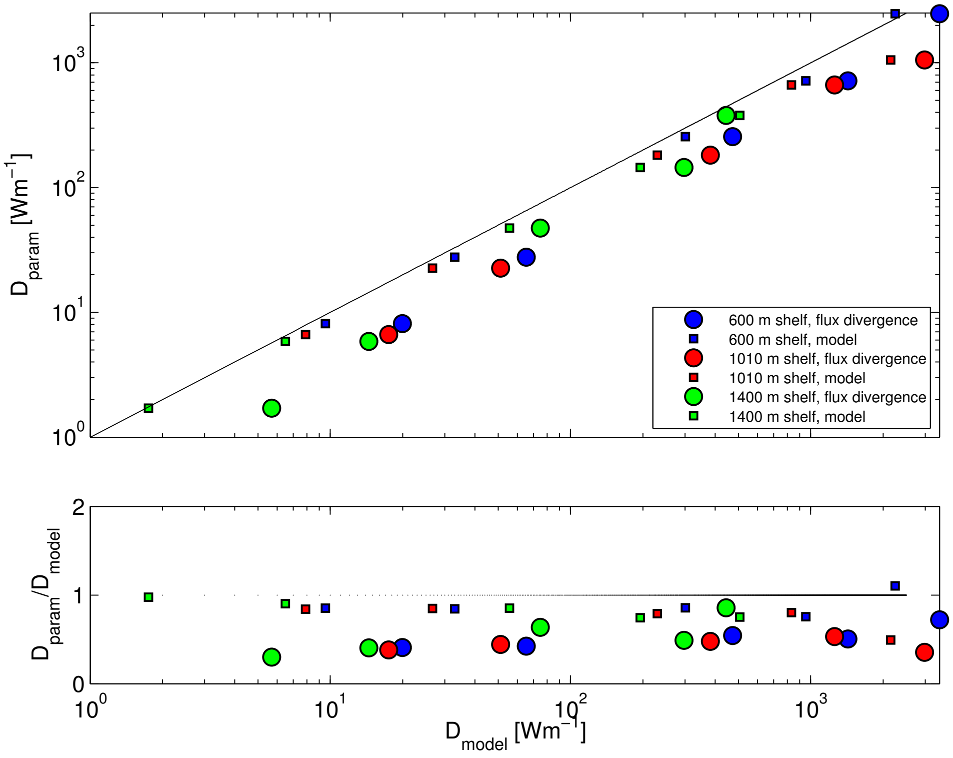

Figure 5.7: Parameterized dissipation D_{param} compared to the dissipation in the numerical model D_{model} for three different shelf heights and five U_0.

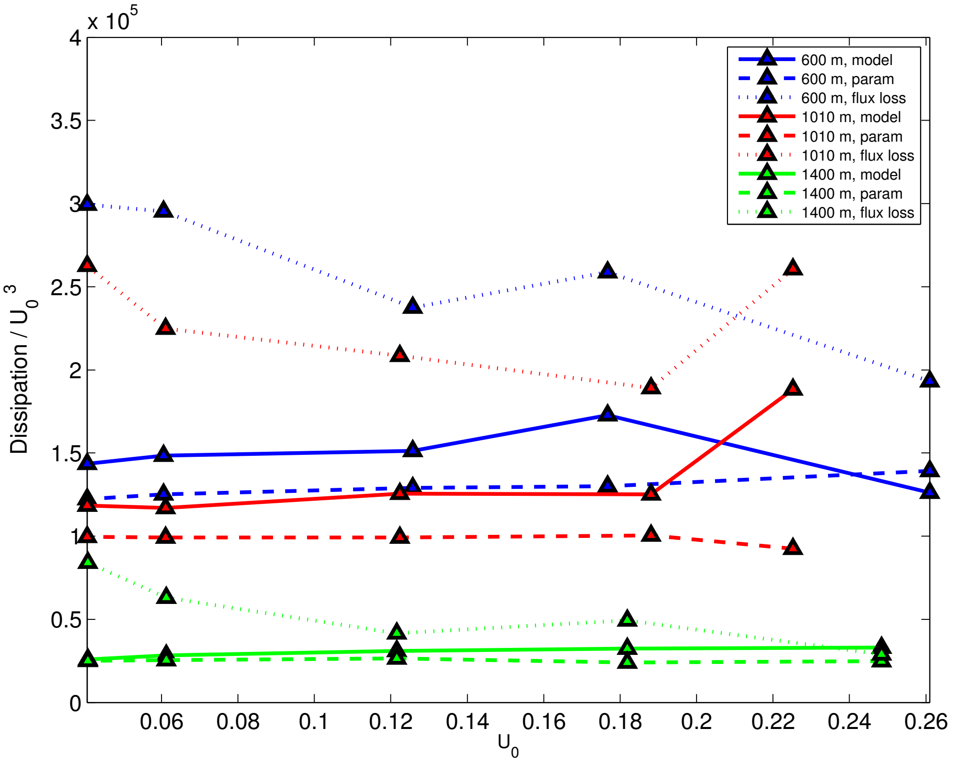

Figure 5.8: Comparison of the dissipation calculated from the model, parameterization, and flux loss scaled by U_0^3 and presented as a function of U_0

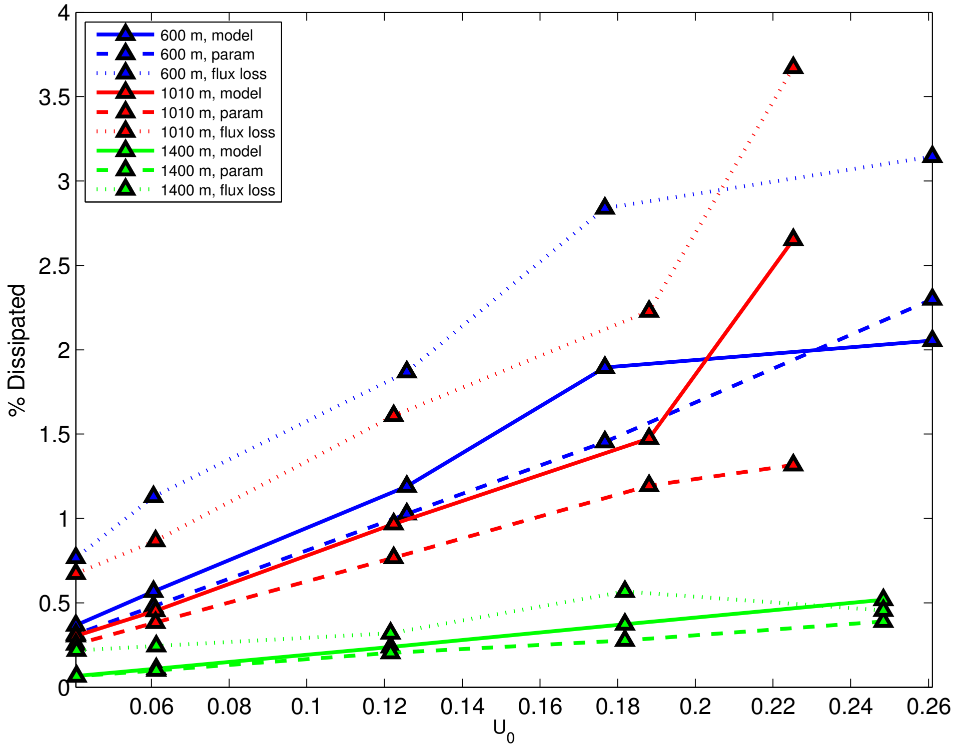

Figure 5.9: The percentage of incoming energy that is dissipated at the shelf break, as a function of U_0

Chapter 6

Discussion of Results

In this thesis, a simple parameterization for dissipation of mode-1 baroclinic tides impacting on an abrupt shelf was presented and compared with numerical model results. Thus far we have illustrated that turbulent dissipation at supercritical shelf topography generated by mode 1 baroclinic tides is localized at the shelf crest. The dissipation at abrupt shelf topography is located at the shelf-break (Figure 3.5) and occurs when the flow is off-shelf (Figure 3.6). The flow off-shelf also creates lee waves, implying that trapped lee waves are a mechanism by which dissipation occurs. The dissipation caused by the trapped lee waves can be reliably predicted *a priori* using linear generation from a step function and assuming all modes with a speed slower than the appropriately averaged baroclinic speed at the shelf crest dissipate locally. The critical mode was determined by iterating through all the modes (Figure 5.5). Each mode was presumed critical and all subcritical modes were averaged over the half wavelength above the shelf crest of the presumed critical mode.

The parameterization recipe tested fairly well against numerical results using idealized topography. Regardless of the shelf height, the parameterization had good predictive ability, although consistently under-estimated flux divergence (Figure 5.7). As forcing U_0 decreased and dissipation approached background levels, the parameterization significantly under-predicted flux dissipation. The flux divergence encounters limitations due to the discretization and numerical techniques applied to the model, but the parameterization is not subject to the same limitations. In addition, the integration of model dissipation can result in over-applying regions of high dissipation. At high forcing U_0, the parameterization is a much closer estimate of the flux divergence. The parameterization chooses c_r and c_t such that the cutoff modes are higher than the cutoff modes that occur in the data (Figure 5.2, Figure 5.3, and Figure 5.4), indicating that the parameterization assumes that fewer modes dissipate than the model demonstrates.

The parameterization shows that a minimal contribution is made to deep ocean mixing by mode-1 waves impacting a continental shelf. We have presented the percentage of incoming energy that dissipates on shelf (Figure 5.9). It is evident that a very small percentage of energy is dissipated at the shelf-break, particularly for a high shelf. The percentage of energy dissipated increases with U_0; however, even for strong forcings the percentage is still very low.

There are a number of errors in the model that contribute to the discrepancy between model and parameterized results. The employed dissipation scheme is known to be limited at small-scale turbulence, leading to inaccurate dissipation and flux divergence. Although the model was run for 10 tidal cycles until dissipation approached steady-state, additional tidal cycles may have ensured that the energetics region of interest was closer to steady-state. The model had a numerical sponge on shelf to absorb all transmitted energy and eliminate any secondary reflection; however, a minimal secondary reflection may have occurred. The sharp, abrupt topography applied to the model also causes unrealistic overturns and dissipation in the model. Error creeps up in the analysis when separating the incoming and reflected tides. The exactness of the fit was dependent on the smoothness of the ellipse, therefore when the system was energetic the ellipse was not completely smooth and the separation was imperfect. The parameterization is also subject to errors. The parameterization does not include barotropic forcing, and although it has been shown to be a small component the barotropic forcing is not negligible, especially when calculating net fluxes. Our analysis has shown that the parameterization predicts mode cutoffs higher than the model demonstrates which will lead to the parameterization under-predicting dissipation, again causing discrepancy between the model and parameterization.

Despite errors the parameterization is good, but there is room for improvement and refinement through further development and testing with model results.

1. The algorithm used to determine the mode cutoffs c_r and c_t has proven insufficient and needs to be refined;

2. All runs were forced in mode-1; however, using forcing in mode-2 and combinations of mode-1 and mode-2 forcing may be more realistic to certain real-world scenarios;

3. The parameterization assumes there is only 1 reflection at the shelf break

whereas it would be valuable to extend the parameterization to include a secondary reflection point;

4. Including a parameter that accounts for the roughness of the topography would allow the parameterization to be more universally applicable.
5. Klymak et al. [2010b] apply a similar parameterization to a barotropic-forced system, thus combining his techniques with the techniques presented would produce a parameterization applicable to systems forced both barotropically and baroclinically.
6. Ultimately, applying the parameterization to in-situ measurements, such as those acquired by Nash et al. [2007] on the Oregon coast would confirm the effectiveness in real-world scenarios.

The findings presented here do not manage to answer the question of what happens to low-mode tidal energy that radiates away from supercritical ridges. The supercritical scattering process has not proven to be an efficient mechanism for dissipation. It is possible, as considered in Klymak et al. [2013], that mode-1 waves move through ocean basins with minimal meaningful interaction with topography. Klymak et al. [2013] note that remote mode-1 internal tides can interfere with generation of new mode-1 tides from the barotropic tide. Such an interference generates a complicated picture of the ocean with mode-1 energy with a nontrivial pathway to turbulence. We have shown that a significant pathway could be dissipation in shallower water; however, the turbulence would not drive deep-ocean mixing. Other potential pathways include small-scale rough topography and near-critical slopes, but regardless of the pathway, low mode internal tides need to be treated on a basin-scale, rather than a local and isolated problem.

Bibliography

C. C. Eriksen. Observations of internal wave reflection off sloping bottoms. *Journal of Geophysical Research*, 1982.

S. M. Kelly, N. L. Jones, J. D. Nash, and A. F. Waterhouse. The geography of semidiurnal mode-1 internal-tide energy loss. *Geophysical Research Letters*, 2013.

J. M. Klymak and S. M. Legg. A simple mixing scheme for models that resolve breaking internal waves. *Ocean Modelling*, 2010.

J. M. Klymak, J. N. Moum J. D. Nash, E. Kunze, J. B. Girton, G. S. Carter, C. M. Lee, T. B. Sandford, and M. C. Gregg. An estimate of tideal energy lost to turbulence at the hawaiian ridge. *Journal of Physical Oceanography*, 2006.

J. M. Klymak, S. Legg, and R. Pinkel. A simple parameterization of turbulent tidal mixing near supercritical topography. *Journal of Physical Oceanography*, 2010b.

J. M. Klymak, M. H. Alford, R. Pinkel, R. C. Lien, Y. J. Yang, and T. Tang. The breaking and scattering of the internal tide on a continental slope. *Journal of Physical Oceanography*, 2011.

J. M. Klymak, M. Buijsman, S. Legg, and R. Pinkel. Parameterizing surface and internal tide scattering and breaking on supercritical topogtaphy: the one- and two-ridge cases. *Journal of Physical Oceanography*, 2013.

P K. Kundu. *Fluid Mechanics*. Academic Press, 1990.

J. Marshall, A. Adcroft, C. Hill, L. Perelman, and C. Heisey. A finite-volume, incompressible navier-stokes model for stuies of the ocean of parallel computers. *J. Geophys. Res*, 1997.

W. Munk and C. Wunsch. Abyssal recipes ii: energetics of tidal and wind mixing. *Deep Sea Research I*, 1998.

J. D. Nash, M. H. Alford, E. Kunze, K. Martini, and S. M. Kelly. Hotspots of deep ocean mixing on the oregon contiental slope. *Geophysical Research Letters*, 2007.

D. L. Rudnick, T. J. Boyd, R. E. Brainard, G. S. Carter, G. D. Egbert, M. C. Gregg, P. E. Holloway, J. M. Klymak, E. Kunze, C. M. Lee, M. D. Levine, D. S. Luther, Martin J. P, M. A. Merrifield, J. N. Moum, J. D. Nash, R. Pinkel, L. Rainfille, and T. B. Sandford. From tides to mixing along the hawaiian ridge. *Science*, 2003.

L. St. Laurent, S. Stringer, C. Garrett, and D. Perrault-Joncas. The generation of internal tides at abrupt topography. *Deep Sea Research*, 2003.

Appendix A

Numerical Techniques

A.1 Mode Decomposition

To perform the complete velocity decomposition it is necessary to start with a time series (for convenience, say 1 tidal period) at a single x-location throughout the depth of the water column. It is important to note that the v velocity data gleaned from the MITgcm model is the net velocity (ie: in the deep basin the difference between the velocity of the incoming and reflected waves). Further processing is necessary to separate the net velocity into incoming and reflected components, which will be described later.

The net velocity data can be described as

$$u(z,t) = u_n(n,t)\mathbf{U_n}(z)$$

where

$$\mathbf{U_n}(z) = \begin{pmatrix} \cos(\frac{z_1\pi}{H}) & \cos(\frac{2z_1\pi}{H}) & ... & \cos(\frac{nz_1\pi}{H}) \\ \cos(\frac{z_2\pi}{H}) & \cos(\frac{2z_2\pi}{H}) & ... & \cos(\frac{nz_2\pi}{H}) \\ \vdots & \vdots & \ddots & \vdots \\ \cos(\frac{H\pi}{H}) & \cos(\frac{2H\pi}{H}) & ... & \cos(\frac{nH\pi}{H}) \end{pmatrix}$$

which can then be rearranged to solve for $u_n(n,t)$. The result is a time series for each mode n. We can further describe each mode as

$$u_n(n,z,t) = a_n \cos(\omega t) \cos\left(\frac{n\pi z}{H}\right)$$

A harmonic fit is then applied to each mode number over the time series. The harmonic fit incorporates amplitude and phase shift information. Using the amplitude and phase information, a new, complex time series can be constructed to more completely describe the same velocity information:

$$v_n(n,t) = \alpha_n e^{i(\omega t + \phi_n)}$$

where α_n is the complex amplitude of the n^{th} mode.

To check to see if the decomposition has worked, the modes can be used as the amplitudes for a summation of cosine curves that reconstruct the raw data from which the decomposition was performed (Figure A.1)

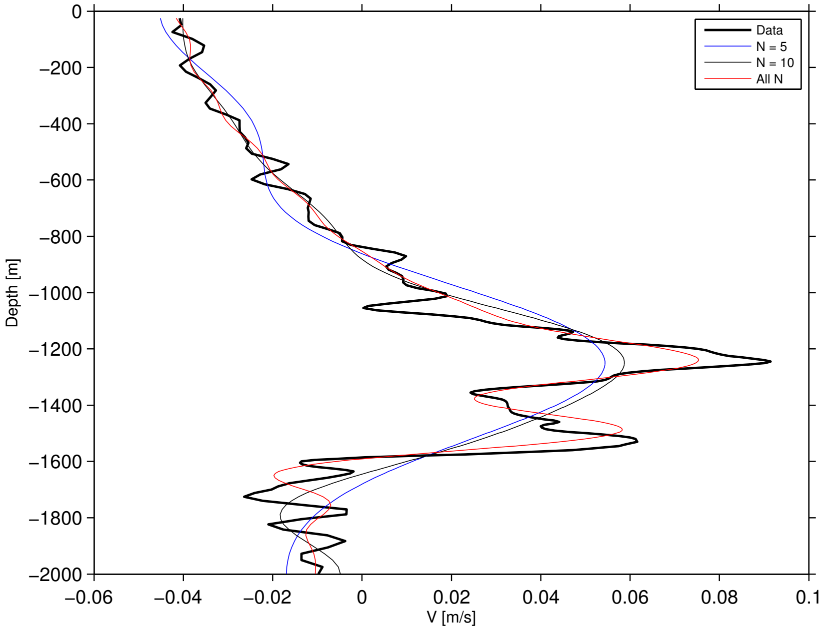

Figure A.1: The net velocity 6 km off-shelf for a 600 m shelf and an incoming velocity of $U_0 = 0.06\,\mathrm{m\,s^{-1}}$, and the reconstruction of the velocity profile by summing modes 1 to 5, 1 to 10, and all modes

A.2 Separation of Incoming and Reflected velocities

Thus far, the velocities used are all net velocities. Using the v net velocity and w net velocity, the net velocities can be separated into incoming and outgoing velocities. It is significant to note that w velocity can be broken into modes in a manner parallel to the v velocity, except that the modes take the form of a sine rather than a cosine. We can assume complex solutions for w and v in the form

$$\begin{aligned} v_n(x,z,t) &= \hat{v}_n(z)e^{i(k_x x-\omega t)} &&= \hat{v}_n \cos\left(\tfrac{n\pi z}{H}\right) e^{i(k_x x-\omega t)} \\ w_n(x,z,t) &= \hat{w}_n(z)e^{i(k_x x-\omega t)} &&= \hat{w}_n \sin\left(\tfrac{n\pi z}{H}\right) e^{i(k_x x-\omega t)} \end{aligned}$$

Therefore, by applying the continuity equation

$$\begin{aligned} \tfrac{du}{dx} + \tfrac{dw}{dz} &= 0 \\ ik_x\hat{u}_n \cos(\tfrac{n\pi z}{H})\cancel{e^{i(k_x x-\omega t)}} + \tfrac{d\hat{w}_n(z)}{dz}\cancel{e^{i(k_x x-\omega t)}} &= 0 \\ \tfrac{d}{dz}\left(\hat{w}_n \sin(\tfrac{n\pi z}{H})\right) &= -ik_x\hat{u}_n \cos(\tfrac{n\pi z}{H}) \\ \hat{w}_n \tfrac{n\pi}{H}\cancel{\cos(\tfrac{n\pi z}{H})} &= -ik_x\hat{u}_n\cancel{\cos(\tfrac{n\pi z}{H})} \\ \hat{u}_n &= i\tfrac{n\pi}{k_x H}\hat{w} \end{aligned}$$

By substituting $k_x = \frac{(\omega^2-f^2)^{1/2}}{c_e}$ and $c_e = HN/n\pi$

$$\hat{u}_n = i\frac{N}{(\omega^2-f^2)^{1/2}}\hat{w}_n$$

For each mode, $\hat{u}$ can be plotted against $\frac{N}{(\omega^2-f^2)^{1/2}}\hat{w}_n$ (or, rather $\hat{w}_{n,s}$) to achieve an ellipse (Figure A.2). The ellipse that is formed is defined as

$$W_n = \hat{u}_n + i\hat{w}_{n,s}$$

and can be fit to

$$W_{n,fit} = a_r(n)e^{i\omega t} + a_i(n)e^{-i\omega t}$$

Fitting the ellipse is equivalent to fitting two circles of different amplitudes, $a_r(n)$ and $a_i(n)$, that progress in opposite directions with time. $a_r(n)$ is the amplitude of the reflected wave, and $a_i(n)$ is the amplitude of the incoming wave.

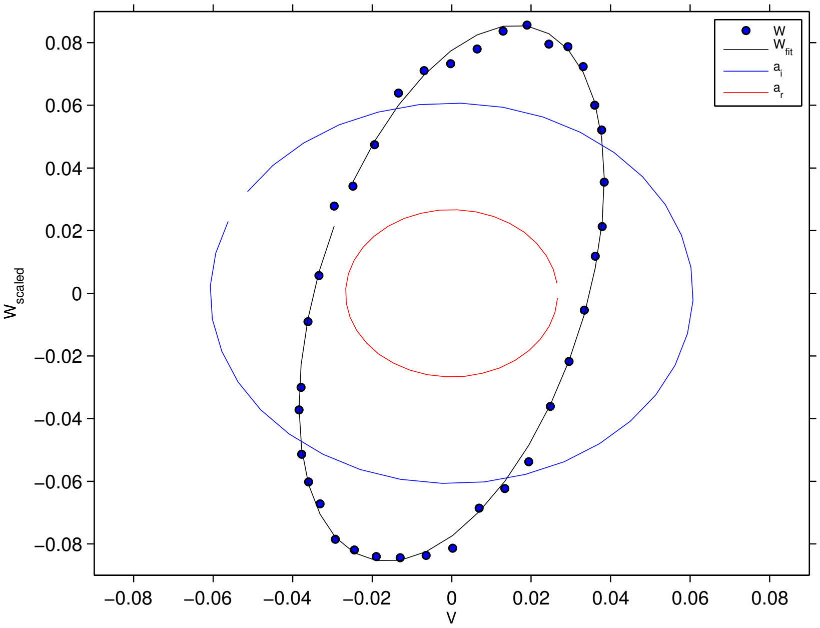

Figure A.2: The ellipse formed 6 km off-shelf for a 600 m shelf and a forcing velocity $U_0 = 0.06\,\mathrm{m\,s^{-1}}$. The blue dots are the scaled velocity data for a single tidal period, the red and blue lines are the circles that are added together to create the ellipse (black line) that is fit to the data. The radius of the red and blue circles is the amplitude of the incoming and reflected wave, respectively.

A.3 Calculating Flux

Before calculating the dissipation, it's necessary to calculate the flux of the reflected and transmitted wave as a function of mode number, n.

$$\begin{aligned}
F(n) &= \int_{-H}^{0} < u(n)p(n) > dz \\
&= \int_{-H}^{0} < \hat{u}(n)\hat{p}(n) > \left(\tfrac{N}{N_0}\right) dz \\
&= \int_{-\hat{H}}^{0} < \hat{u}(n)\hat{p}(n) > \left(\tfrac{N}{N_0}\right)\left(\tfrac{N_0}{N}\right) d\hat{z} \\
&= \int_{-\hat{H}}^{0} < \hat{u}(n)\tfrac{g(\omega)}{m(n)}\hat{u}(n) > d\hat{z} \\
&= \tfrac{g(\omega)}{m(n)} \int_{-\hat{H}}^{0} < \hat{u}^2(n) > d\hat{z}
\end{aligned}$$

where the flux is converted to WKB values by using the conversion factors $u = (N/N_0)^{1/2}\hat{u}$, $p = (N/N_0)^{1/2}\hat{p}$, $dz = (N_0/N)d\hat{z}$, and $\hat{p}(n) = g(\omega)/m(n)$. In this case

$$g(\omega) = \rho\frac{[(N_0^2 - \omega^2)(\omega^2 - f^2)]^{1/2}}{\omega}$$

$$m(n) = \frac{n\pi}{\hat{H}}$$

Therefore, by using the reflected and transmitted velocities defined above, the flux is calculated as a function of mode for the reflected and transmitted waves:

$$\begin{aligned}
< u_r^2(n) > &= \tfrac{\omega}{2\pi} \int_0^{2\pi/\omega} Re\left\{\cos\left(\tfrac{n\pi\hat{h}}{\hat{H}}\right) a_r(n)e^{i(kx-\omega t)}\right\}^2 dt \\
&= \tfrac{\omega}{2\pi} \int_0^{2\pi/\omega} \cos^2\left(\tfrac{n\pi\hat{h}}{\hat{H}}\right) a_r^2(n)\cos^2(\omega t)dt \\
&= \tfrac{\omega}{2\pi} \cos^2\left(\tfrac{n\pi\hat{h}}{\hat{H}}\right) a_r^2(n)\tfrac{\pi}{\omega} \\
&= \tfrac{1}{2}\cos^2\left(\tfrac{n\pi\hat{h}}{\hat{H}}\right) a_r^2(n) \\
F_r(n) &= \tfrac{g(\omega)}{2m(n)} \int_{-\hat{H}}^{0} \cos^2\left(\tfrac{n\pi\hat{z}}{\hat{H}}\right) a_r^2(n)d\hat{z} \\
&= \tfrac{g(\omega)}{2m(n)}a_r^2(n) \int_{-\hat{H}}^{0} \cos^2\left(\tfrac{n\pi\hat{z}}{\hat{H}}\right) d\hat{z} \\
&= \tfrac{g(\omega)}{2m(n)}a_r^2(n)\tfrac{\hat{H}}{2} \\
&= \hat{H}\tfrac{g(\omega)}{2m(n)}\tfrac{a_r^2(n)}{4}
\end{aligned}$$

Similarly,

$$F_t(n) = \hat{h}\frac{g(\omega)}{2m(n)}\frac{a_t^2(n)}{4}$$

The flux of the incoming and reflected components show that more energy is in mode-1 of the incoming component than in mode-1 of the reflected component

(Figure A.3).

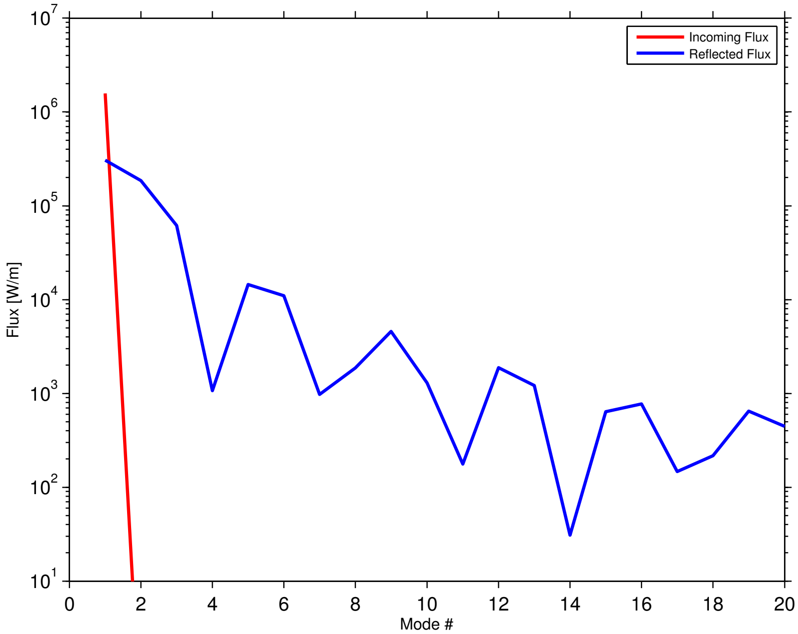

Figure A.3: The incoming and reflected flux 6 km off-shelf for a 600 m shelf and a forcing velocity of $0.06\,\mathrm{m\,s^{-1}}$